A COMBINED CFD-DSMC METHOD FOR NUMERICAL SIMULATION OF NOZZLE PLUME FLOWS

A Dissertation
Presented to the Faculty of the Graduate School
of Cornell University
in Partial Fulfillment of the Requirements for the Degree of
Doctor of Philosophy

by
Jyothish D George
January 2000

The objective of this dissertation was to develop a methodology for performing simulations of a complete nozzle plume system. The combined approach involves four steps. First, a continuum simulation of the nozzle plume system is performed. An unstructured Navier-Stokes solver for performing these simulations was developed. The next step involves predicting the breakdown of Navier-Stokes equations from the CFD simulations and dividing the domain into a CFD region and a DSMC region. Various parameters that could be used for this were investigated and a new parameter was proposed. The third step involves transferring information from the CFD simulation to the DSMC simulation. Different methods of transferring information were analyzed. The last step involves performing DSMC simulations. DSMC simulations were performed and the results were analyzed to understand more about the breakdown of the Navier-Stokes equations.

The method was applied to the study of two nozzle systems for which experimental results were available. The first system involved was a hydrogen thruster. A kinetics model for hydrogen consistent with a previously developed DSMC model was implemented. It was successfully applied to investigate the low-density hydrogen plume flows. The comparison between the numerical results and experimental measurements was found to be good in terms of overall flow features. For a more detailed quantitative comparison higher resolution experimental measurements are required. An important conclusion of this study is that these solutions exhibit a high degree of grid dependence. This was found to be true of both the DSMC and

CFD computations. Thus care should be taken to ensure that the grid resolution is fine enough to obtain accurate results. This emphasizes the importance of flexible gridding techniques provided by the use of unstructured grids. For this system, it is difficult to separate the results of the grid dependence from the physics of the problem.

The next system analyzed was the expansion of carbon di-oxide into vacuum. The computational results were found to be sensitive to the wall boundary condition. Experimental measurements of pitot pressure measurements along the centerline were compared with calculations based on the CFD simulations. The computed values were close enough to experimental measurements to suggest that the physics of the flow was captured accurately. Detailed relaxation modeling of the different energy modes of CO_2 indicated that the vibrational mode was frozen in the diverging portion of the nozzle and in the plume. The CFD simulations also predicted regions of rotational non-equilibrium inside the plume. The central core region of the flow was non-isentropic and had a ratio of specific heats, γ close to 1.2. This invalidates the isentropic flow assumption and the value of γ of 1.4 used for calibrating some of the experimental measurements. The computations re-confirmed earlier findings about the behavior of the flow near the nozzle lip. Flow angle measurements were compared with the computed values and found to agree in the central-core region of the flow. The CFD predictions of radial profiles of number density showed good agreement within regions of validity of the continuum approach.

A breakdown parameter was used to split the domain by predicting the breakdown of the Navier-Stokes equations. DSMC simulations were performed of regions where CFD methods are not accurate, were performed. The DSMC predictions of radial number density profiles were then compared with the experimental measurements and found to be in good agreement, even in regions where the CFD results disagree with experiments. DSMC results were analyzed in detail in an attempt to investigate the failure of the CFD approach. It was found that the regions where CFD results are inaccurate corresponded with regions of translational non-equilibrium. Since the Navier-Stokes equations are based on the assumption of translational equilibrium, solutions to Navier-Stokes equations give inaccurate results for such flow regimes.

Biographical Sketch

This is dedicated to my mother and father, sisters and brothers, aunts and uncles, cousins, grandparents, etc. Oh yes, and my 6th grade math teacher who thought I would never get past 7th grade math.

Acknowledgements

I would like to acknowledge the fantastic help and support of all of those who helped and supported me. Without their tireless help and support I would have not been able to do this fine work.

Finally, I gratefully acknowledge the efforts of Dr. James Drakes in being instrumental in the release of the AEDC report for public distribution. This research has been supported by the Army Research Office Grant DAAG55-98-1-0500 and by NASA Lewis Research Center Grant NAG3-1958.

Table of Contents

List of Tables

List of Figures

Chapter 1

Motivation and Background

This chapter presents the motivation behind this work and the scope of this work.

1.1 Introduction

Small rockets are used extensively for attitude control and other low thrust operations on trans-atmospheric vehicles and spacecraft. They are also used in satellites for station keeping and various other operations. Low thrust electric thrusters and a variety of chemical thrusters are being developed for these applications.

There a two main concerns involving the use of these thrusters. The first issue is their efficiency. These nozzles are typically inefficient because of their small size, which leads to losses due to viscous and non-equilibrium effects. Another important issue is the effect of the exhaust plume impingement on the spacecraft. Plume impingement on the vehicle surface may lead to unwanted heating of the surface. The solar arrays and electronic devices may lose effectiveness under long term exposure to rocket exhaust gases. These gases might contaminate the thermal protection systems of trans-atmospheric vehicles. Impact of the plume on the spacecraft might also produce unwanted torques or thrust losses. An accurate assessment of these issues requires detailed understanding of the fluid dynamics and kinetics of the nozzle and plume flow. With this in mind, several experimental and numerical studies have been directed towards the prediction and characterization of such flows.

Numerical investigations of all the issues involved in using these thrusters require accurate modeling of the complete nozzle plume system. Such investigations are challenging because of the range of flow regimes involved. The flow regimes are generally characterized by the Knudsen number, which can be defined as the ratio of the mean free path to a characteristic length of the flow field. The Knudsen number inside the nozzle is usually much less than one and this regime is referred to as the continuum flow regime. As the flow expands the densities become lower and lower and soon the Knudsen numbers are large enough for the flow to transition into the non-continuum regime. In the continuum regime the flow physics is described by the Navier-Stokes formulation.

As the low-density effects become important there is considerable uncertainty as to whether the continuum Navier-Stokes formulation adequately describes the underlying physics. This had led researchers to take an alternative point of view and simulate flows directly using Monte Carlo methods based on the molecular theory of gases. The Direct Simulation Monte Carlo method developed by Bird has been successfully used to simulate nozzle plume flows[1,2,3,4,5]. Although Monte Carlo methods are efficient for very rarefied flows, they are prohibitively expensive in the continuum regime. Thus from the point of view of performing simulations of the complete nozzle plume system, Monte Carlo methods are accurate and reliable but very expensive while the continuum Navier-Stokes equations coupled with thermo-chemical non-equilibrium tools are solved rather efficiently but of questionable validity in the very rarefied flow regimes.

Thus an approach using any one of these methods has limitations which would prevent performing simulations of the complete system. This dissertation looks at the possibility of using a combined approach and investigates the various steps involved in pursuing such an approach.

1.2 Objectives and Scope of this work

Figure 1.1 shows a schematic of the nozzle plume system. The basic objective of this dissertation is to investigate numerical approaches to studying this system and develop an efficient and accurate method for performing such simulations.

A Navier Stokes solver that can be used to perform simulations of these systems needs to be developed. Since these flows have complicated geometries and complex flow gradients, an unstructured grid solver would be most efficient. The breakdown of Navier-Stokes solvers would be analyzed in detail to understand the reason for their failure and predict their failure accurately. The methodology needs to be validated by comparing with experimental measurements. The focus of this work is on developing and validating the methodology.

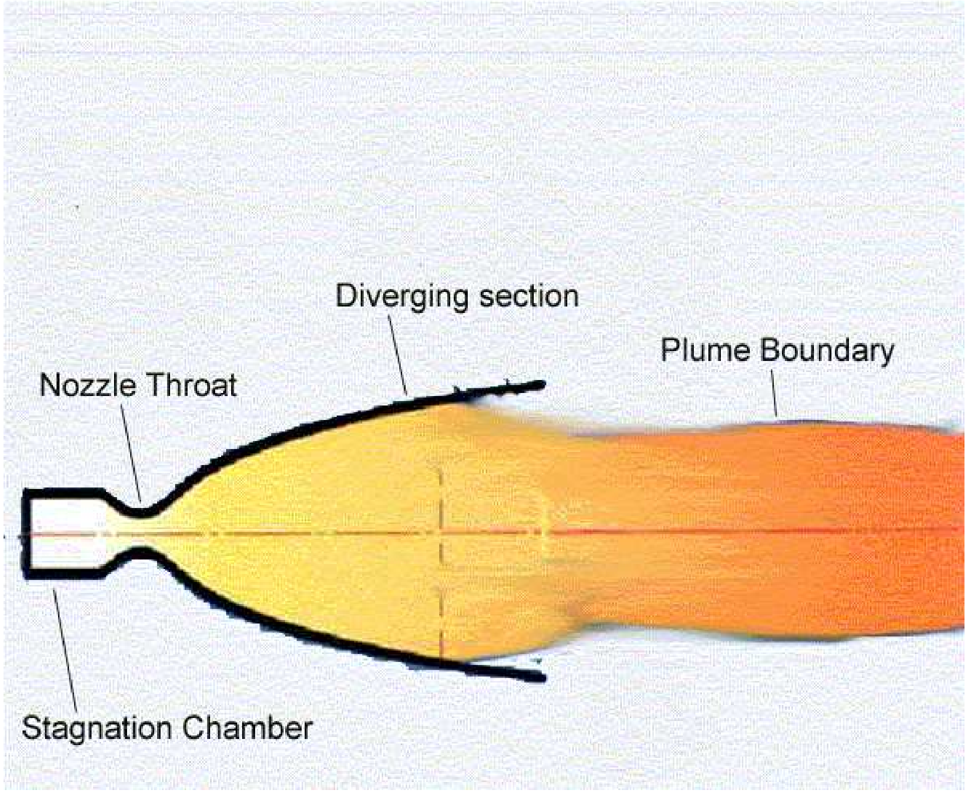

Figure 1.1. Schematic of the nozzle plume system

Chapter 2

Description of the combined approach

This chapter presents an outline of this work and a brief description of the rest of the thesis.

2.1 Introduction

The objective of this study is to develop a method for performing numerical simulations of a complete nozzle plume system for small rockets. Computer simulations of the complete system from the inlet of the nozzle to the outer plume regions are difficult to perform because of the wide range of Knudsen numbers involved. The comparatively high-density flow inside the nozzle is most appropriately modeled using a continuum based Computational Fluid Dynamics (CFD) approach. The CFD method has physical and numerical limitations that prevent it from being used for very rarefied flows. Since the outer plume and back-flow regions involve very low densities, the direct simulation Monte Carlo (DSMC) method is used in these regions. However, the DSMC method cannot be used for the full system, as it is very expensive for simulating the comparatively high number densities inside the nozzle. Thus an efficient and accurate numerical approach requires a combination of these two methods. This thesis describes the development of such a combined approach. The method is validated by applying it to the study of two systems for which experimental results are available.

2.2 Description of methodology

The simplest combined approach involves splitting the domain into two and performing two de-coupled simulations. The CFD method is used for the nozzle and near plume regions while the DSMC method is used for the outer plume regions. The CFD solution is used to prescribe boundary conditions for the DSMC code.

This combined approach involves three steps. The first step is developing and implementing a Navier-Stokes solver for performing simulations of the nozzle and near plume region. The next step is developing parameters for determining the extent of the CFD domain by predicting the breakdown of the CFD method. The third step is developing mechanisms for transferring information from the CFD simulations to the DSMC simulations at the interface and performing DSMC simulations. DSMC codes capable of performing simulations of the plume already exist.

2.3 CFD Simulations

The CFD simulations are performed using an unstructured finite volume Navier-Stokes solver. The CFD code is based on a cell centered finite volume formulation that can be used on unstructured triangular or quadrilateral meshes. The equations being solved are the Navier-Stokes equations expanded so as to include thermo-chemical effects. The code takes into account rotational relaxation effects, vibrational relaxation effects and chemical reactions. The details of the kinetics model need to be implemented separately for each application. The convective fluxes are calculated based on an upwinding method originally developed by MacCormack and Candler[21] for structured grids. The implementation of the upwinding method for unstructured grids is similar to the one described by Batina.[22] The computation of gradients at each control volume is performed using Green-Gauss integration around the control volume boundary.[23] A weighting process[24] is used to improve accuracy so that in a regular triangular mesh made of equilateral triangles the gradient is second order accurate. The code uses an explicit method for time stepping and uses local time stepping to accelerate convergence.

2.4 Chapman-Enskog Parameter

Existing parameters for predicting continuum breakdown have two major limitations. The value of the parameter at which breakdown is assumed to occur is arbitrary. Also, they do not have a very strong theoretical basis. A new parameter is proposed in this thesis. It is based on the assumptions made during the derivation of the Navier-Stokes equations from the Boltzmann equation. This parameter based on the Chapman-Enskog expansion is used to predict failure of the Navier-Stokes solver.

2.5 DSMC Simulations

The DSMC method employs a large number of model particles to simulate the behavior of the actual gas molecules. Due to the nature of the simulation method, DSMC is capable of capturing nonequilibrium effects. The technique has been successfully applied to model nozzle and plume flows expanding from small rockets[1, 2,3,4,5]. In this study DSMC simulations were performed using a parallel, optimized implementation of the Direct Simulation Monte Carlo algorithm[17]. It is a large system called "MONACO" based on a DSMC algorithm formulated specifically for workstation architectures. The DSMC simulations use results from the CFD simulations as boundary conditions.

2.6 Outline of thesis

This section gives a brief outline of the rest of the thesis. Chapter three gives a detailed description of the continuum code developed for this study. Chapter four gives a brief description of the DSMC code used for the study. The DSMC code has been used extensively before and is described in detail by Dietrich & Boyd[17]. The first step in this study is the validation of the CFD code. The code is validated by performing simulations of a hydrogen plume system. Experimental studies on this system were conducted at Stanford University[19]. The results of the validation study are presented in chapter five. The hydrogen system was found to be unsuitable for demonstrating the advantages of using a combined methodology. The experimental measurements of that system were not of sufficient resolution to show a clear difference between the CFD computations and DSMC computations.

The next few chapters deal with the study of another experimental system involving carbon di-oxide expansions into vacuum. This system was studied in detail through experimental investigations conducted at Arnold Engineering Research Center[9]. Tabel 2.1 shows the details of the two systems.

The nozzle and near plume simulations of a carbon dioxide system are described in chapter six. Chapter seven looks at different continuum breakdown parameters. Experimental measurements that agree with DSMC computations and disagree

	Flow rate	**Area Ratio**	ϕ	T_0	**Re**	**Kn**
Gas	[Kg/m/s]		**[Degrees]**	**[Kelvin]**		
H_2	1	$7.8 \cdot 10^{12}$	7.2	9.2	0.0	0.0
CO_2	3	$6.5 \cdot 10^{15}$	10.3	2.4	0.0	0.0

Table 2.1. The two systems investigated in this study.

with CFD computations are used to clearly demonstrate the breakdown of the continuum approach. An analysis of the DSMC results is presented to investigate the reasons behind the failure of the Navier-Stokes solver. Chapter eight presents results of DSMC computations of the back-flow region. The last chapter presents the conclusions of the study and suggestions for future work.

Chapter 3

Development of Unstructured grid solver

This chapter presents the underlying assumptions, the governing equations and the numerical approach followed for developing the continuum code.

3.1 Introduction

The continuum code solves the set of coupled partial differential equations that describes the dynamics of the flow field. The equation set is the Navier-Stokes equations expanded to include finite rate relaxation processes. The formulation assumes a generic problem, *i.e.* a gas mixture with rotational relaxation effects, vibrational relaxation effects and chemical reactions.

The continuum formulation assumes that the Knudsen number, which can be defined as the ratio of the mean free path associated with the flow to the characteristic length scale of the body or the flow itself, is much less than one. In addition to the equations of conservation of mass, momentum and energy, the shear stresses, heat flux and diffusion velocities need to be expressed in terms of lower-order macroscopic properties. These constitutive relations for the viscous stress tensor, the heat flux vector, and the diffusion velocity of species in terms of gradients of the flow are assumed to be linear. The thermal state of the gas is assumed to be described by separate and independent temperatures. The energy in the translational modes is assumed to be characterized by a single temperature referred to as the translational temperature. This assumption of translational equilibrium is critical to the continuum formulation. A rotational temperature characterizes the energy contained in the rotational mode. All vibrational modes are represented by a single vibrational temperature. The vibrational mode is assumed to conform to the harmonic oscillator description at all vibrational temperatures. This is accurate at low vibrational levels, but becomes suspect at high vibrational temperatures where the vibrational states may be non-harmonic. However the energy contained in these states are negligible for the flowfields of interest in this study.

3.2 Mathematical formulation

The governing equations are basically the Navier-Stokes equations of gas dynamics. To account for the non-equilibrium processes considered, a partial differential equation is added for each energy mode considered. These equations are described in detail in this section.

3.2.1 Conservation equations

The equations are presented in their Cartesian tensor notation for simplicity, although two-dimensional axisymmetric equations are used in this study. The conservation of mass is replaced by a species equation for each individual species due to chemical nonequilibrium. For a gas made up of ns species there would be ns species continuity equations. The species continuity equation, which states the conservation of mass, for any species i in the gas mixture is given by

$$\frac{\partial \rho_i}{\partial t} + \frac{\partial(\rho_i u_k + j_{ik})}{\partial x_k} = \omega_i, \tag{3.1}$$

where ρ_i is the density of species i , u_k is the velocity component in the k direction and $j_{i,k}$ is the diffusive mass flux of species i in the k direction. ω_i is the source term for species i and it represents the rate of production of species i due to chemical reactions.

The mass averaged momentum equation, which gives the conservation of momentum in a gas mixture, is given by

$$\frac{\partial \rho u_j}{\partial t} + \frac{\partial(\rho u_j u_k + \tau_{jk} + p\delta_{jk})}{\partial x_k} = 0. \tag{3.2}$$

Here ρ is the density of the flow, while u_i, u_j, u_k are velocity components in the i, j, and k directions, $\tau_{i,j}$ is a component of the shear stress tensor, p is pressure and $\delta_{j,k}$ is the delta function.

Two additional energy equations are introduced to account for thermal nonequilibrium processes *i.e.* the relaxation of vibrational and rotational degrees of freedom. The conservation of vibrational energy within a diatomic species is as follows

$$\frac{\partial E_v}{\partial t} + \frac{\partial(u_k E_v + q_{vk})}{\partial x_k} = \omega_v, \tag{3.3}$$

where E_v is the energy in the vibrational mode, q_{vk} is the heat flux associated with the vibrational mode in the k direction, u_k is the velocity component in the k direction and ω_v is the vibrational source term.

The conservation of rotational energy is expressed

$$\frac{\partial E_r}{\partial t} + \frac{\partial(u_k E_r + q_{rk})}{\partial x_k} = \omega_r, \tag{3.4}$$

where where E_r is the energy in the rotational mode, q_{rk} is the heat flux associated with the rotational mode in the k direction and ω_r is the rotational source term.

Finally the conservation of total energy is stated by

$$\frac{\partial E}{\partial t} + \frac{\partial((E+p)u_k + q_k u_j \tau_{jk})}{\partial x_k} = 0, \tag{3.5}$$

where E is the total energy, and q_k is the total heat flux in the k direction, while u_i, u_j, u_k are velocity components in the i, j, and k directions, $\tau_{i,j}$ is the component of the shear stress tensor and p is pressure.

3.2.2 Equations of state

The equations of state used to calculate the non-conserved quantities from the conserved quantities are presented now. The equation of state for pressure of the gas mixture is given by

$$p = \rho R T, \tag{3.6}$$

where ρ is the density and R is the gas constant and T is the temperature.

The total energy per unit volume, E, is made up of the various modes of internal energy, *i.e.* translational, rotational, vibrational, the kinetic energy of the flow and the energy arising from the formation of the species. Therefore the total energy per unit volume for a gas with ns species is given by

$$E = C_v \rho T + E_v + E_r + \frac{1}{2}\rho(u^2 + v^2) + \sum_{i=1}^{ns} \rho_i h_i^0 \tag{3.7}$$

Here C_v is the specific heat at constant volume, T is the temperature, E_v and E_r represent the energy contained in the vibrational and rotational modes, ρ is the density of the gas and u and v are the velocity components in the x and y direction and h_i^0 is the heat of formation of species i.

The vibrational energy in any diatomic species i is expressed by

$$E_{vi} = \rho_i \frac{R}{M_i} \frac{\theta_{vi}}{e^{(\frac{\theta_{vi}}{T_v})} - 1}), \tag{3.8}$$

where θ_{vi} is the characteristic temperature for vibration, M_i is molecular weight of species i and T_v is the vibrational temperature. The rotational energy is represented by

$$E_{ri} = \rho_i \frac{R}{M_i} T_r, \tag{3.9}$$

where T_r is the rotational temperature. The vibrational temperature of the individual species is determined by inverting the expression for vibrational energy contained in a simple harmonic oscillator at the temperature. This inversion is done using an iterative procedure using Newton's method. The rotational temperature is obtained from the Eq.(3.9) .

3.2.3 Shear stresses, Heat fluxes and Diffusion velocities

In the Navier Stokes formulation the diffusive fluxes are linearly related to the gradients of the associated flow quantities. Thus from the Newtonian fluid assumption the shear stress tensor can be related to the velocity gradient tensor by the expression

$$\tau_{ij} = -\mu(\frac{\partial u_i}{\partial x_j} + \frac{\partial u_j}{\partial x_i}) - \lambda \frac{\partial u_k}{\partial x_k} \delta_{i,j} \tag{3.10}$$

with the Stokes hypothesis

$$\lambda = \frac{-2}{3}\mu. \tag{3.11}$$

Here $\tau_{i,j}$ is the component of the shear stress tensor, u_i is the component of velocity in the i direction and $\delta_{i,j}$ is delta function. μ is the coefficient of viscosity and is calculated for each species using the viscosity model for a reacting gas developed by Blottner[6]. The model uses a curve fit with three constants to give

$$\mu_s = 0.1 exp[(A_s lnT + B_s) lnT + C_s], \tag{3.12}$$

in kg/m s, as a function of temperature T. The constants, A_s, B_s and C_s need to be specified for the each gas species. For some of the applications presented in this thesis this model has been replaced by a model developed for DSMC methods where the dependence of μ with temperature is specified. These models are described in the subsequent chapters. The total viscosity of the gas is then calculated using Wilke's semi-empirical mixing rule[7].

Fourier's law of heat conduction gives the heat flux vector, q_ϕ associated with energy mode ϕ to the gradient of temperature T_ϕ

$$q_j = -\kappa_\phi \frac{\partial T_\phi}{\partial x_j}. \tag{3.13}$$

Here κ_ϕ is the thermal conductivity associated with T_ϕ. The conductivity of the rotational and vibrational temperatures for each species may be derived from the Eucken relation[8]. With this formulation it is assumed that the transport of translational energy involves a correlation with the velocity, but the transport of internal energy (rotational and vibrational) involves no correlation with velocity. The thermal conductivity for translational energy, κ_t, is

$$\kappa_t = \frac{5}{2}\mu C_{v_t}, \tag{3.14}$$

where μ is the coefficient of viscosity and C_{v_t} is the specific heat at constant volume for translational energy. The total thermal conductivity of the gas is then calculated using Wilke's semi-empirical mixing rule[7].

Similarly Ficks law of diffusion give the diffusive mass fluxes for species s as

$$\rho_s v_{sj} = -\rho D_s \frac{\partial c_s}{\partial x_j}, \tag{3.15}$$

where ρ_s is the density of the species, v_{sj} is the diffusion velocity, and c_s is the mass fraction of the species s . The diffusion coefficient D_s is derived by assuming a constant Lewis number, Le which by definition is given by

$$Le = \frac{D\rho c_p}{\kappa}, \tag{3.16}$$

where ρ is density, C_p specific heat at constant volume and κ is the coefficient of thermal conductivity.

3.2.4 Energy exchange mechanisms

Vibration translation (V-T) energy exchange is the process by which energy is exchanged between the vibrational and translational modes. This process appears as source terms in the conservation equation for the vibrational energy mode. The Landau-Teller form of vibrational relaxation represents a V-T energy transfer and describes how the system of oscillators approaches its equilibrium state. These energy transfers appear as source terms in the equations described above. The source terms in the vibrational energy equation for any molecular species i is assumed to be

$$w_{vi} = \frac{E_{vi}^* - E_{vi}}{\tau_{vi}} \tag{3.17}$$

, where E_{vi} is vibrational energy per unit volume and τ_{vi} is the vibrational relaxation time. E_{vi}^* is the vibrational energy evaluated at the local translational temperature. The source terms in the rotational energy equation are similar to those in the vibrational energy equation. The rotation-translation energy mechanism would be

$$w_{ri} = \frac{E_{ri}^* - E_{ri}}{\tau_{ri}}, \tag{3.18}$$

where E_{ri} is rotational energy per unit volume and τ_{ri} is the rotational relaxation time. Similarly E_{ri}^* is the rotational energy evaluated at the local translational temperature.

3.3 Numerical method

Traditionally structured methods that rely on regular array of quadrilateral cells have been used to solve such problems. Recently, unstructured grid methods have emerged as a viable alternative to discretizing complex geometries. These methods provide greater flexibility for discretizing complex domains and also enable straightforward implementation of adaptive meshing techniques. Since these flows have complicated gradients that need to be captured accurately, the continuum method is formulated for unstructured grids. Since the DSMC code also uses unstructured grids this simplifies the division of the domain between the two methods and also facilitates communication between the two methods.

The conservation law form of the two dimensional (or axi-symmetric) Navier-Stokes equations, with n chemical species including chemical and thermal nonequilibrium (m separate vibrational modes) processes, in the Cartesian coordinates can be written as

$$\frac{\partial U}{\partial t} + \frac{\partial (F + F_v)}{\partial x} + \frac{\partial (G + G_v)}{\partial y} = W, \tag{3.19}$$

, where U is the state vector, F and G are the convective flux vectors, F_v and G_v are the diffusive flux vectors, and W is the source term vector. The state vector U, the convective flux vectors F and G, are defined as follows:

$$U = \begin{pmatrix} \rho_1 \\ \rho_2 \\ \vdots \\ \rho_n \\ \rho u \\ \rho v \\ E_{v1} \\ E_{v2} \\ \vdots \\ E_{vm} \\ E_r \\ E \end{pmatrix}, F = \begin{pmatrix} \rho_1 u \\ \rho_2 u \\ \vdots \\ \rho_n u \\ \rho u^2 + p \\ \rho uv \\ uE_{v1} \\ uE_{v2} \\ \vdots \\ uE_{vm} \\ uE_r \\ u(E+p) \end{pmatrix}, G = \begin{pmatrix} \rho_1 v \\ \rho_2 v \\ \vdots \\ \rho_n v \\ \rho uv \\ \rho v^2 + p \\ vE_{v1} \\ vE_{v2} \\ \vdots \\ vE_{vm} \\ vE_r \\ u(E+p) \end{pmatrix}.$$

$$F_v = \begin{pmatrix} \mathrm{J}1_x \\ \mathrm{J}2_x \\ \vdots \\ \mathrm{J}n_x \\ \tau_{xx} \\ \tau_{yx} \\ q_{v_{1_x}} \\ q_{v_{2_x}} \\ \vdots \\ q_{v_{m_x}} \\ q_{r_x} \\ u\tau_{xx} + v\tau_{yx} + q_x \end{pmatrix}, G_v = \begin{pmatrix} \mathrm{J}1_y \\ \mathrm{J}2_y \\ \vdots \\ \mathrm{J}n_y \\ \tau_{sy} \\ \tau_{yy} \\ q_{v_{1_y}} \\ q_{v_{2_y}} \\ \vdots \\ q_{v_{m_y}} \\ q_{r_y} \\ v\tau_{yy} + u\tau_{xy} + q_y \end{pmatrix}, W = \begin{pmatrix} \omega_1 \\ \omega_2 \\ \vdots \\ \omega_n \\ 0 \\ 0 \\ \omega_{v1} \\ \omega_{v2} \\ \vdots \\ \omega_{vm} \\ \omega_r \\ 0 \end{pmatrix}$$

are the viscous (diffusive) fluxes F_v and G_v, and the source vector, W.

Here the flux vector is split into an inviscid flux vector and a viscous flux vector. In the integral form for a control volume V(t) with boundary S(t) the governing equations are given by

$$\frac{\partial}{\partial t}\int_{V(t)} W dv + \oint_{S(t)} (F\vec{i} - G\vec{i}) \cdot \vec{n} dl + \oint_{S(t)} (F_v\vec{i} - G_v\vec{i}) \cdot \vec{n} dl = 0. \tag{3.20}$$

Since the domain is subdivided into polygonal elements the semi-discrete form of this equation is given by

$$\Omega_s \frac{\partial W}{\partial t} = -\sum_{s=1}^{n} H_s \Delta l_s, - -\sum_{s=1}^{n} H_{v_s} \Delta l_s, \tag{3.21}$$

where Ω_s denotes the volume of the cell, H_s is a numerical approximation to the normal convective flux crossing a face s with side length Δl_s and n is the number of sides of the polygon. H_{v_s} is the corresponding viscous flux. H_s and H_{v_s} can be obtained by rotating the flux terms in Eq. 3.10 as follows

$$H = F\vec{i} - G\vec{i}. \tag{3.22}$$

The expression for the flux F_s at the interface can be calculated by a number of upwind methods. It should noted that it is now a one dimensional problem where the flux normal to the face is being evaluated. In this implementation, it is performed using the flux-vector splitting proposed by MacCormack, which is briefly explained here.

The computation of the inviscid flux terms are based on an upwinding technique. Upwinding techniques model the underlying physics better than more conventional centered methods. The upwinding method used was developed for structured grids by MacCormack and Chandler[21]. They successfully applied it to the investigation of numerous hypersonic flows. The details of their method are described in Chandler's thesis[8]. The implementation of the upwinding method for unstructured grids is similar to the one described by Batina.[22]

Evaulation of the inviscid part involves calculating the term $\oint_{S(t)} (F\vec{i} - G\vec{i}) \cdot \vec{n}dl$ in the previous equation.

The convective flux is assumed to have two parts $F = F_+ + F_-$, where F_+ is the flux associated with the right running waves, and F_- with the left running waves. The splitting of the flux vector is not unique and many possibilities for splitting exist. In this implementation we use the MacCormack-Chandler scheme which is a variation of the Steger-Warming scheme. The splitting is based on an approximate solution of the Riemann problem in one dimension. In the Steger Warming type flux vector splitting, we make use of the fact that the convective flux vector is homogenous of degree one in U, i.e., F=AU, where A is the Jacobean of F with respect to U. The matrix A can be diagonalized using similarity transformations such that $A = S^{-1}C_A^{-1}\Lambda C_A S$. Chandler describes these matrices S, C_A , S^{-1}, and C_A^{-1} in detail[8]. A can now be split into two parts depending on the sign of the eigenvalues

$$A_+ = S^{-1}C_A^{-1}\Lambda_+ C_A S \tag{3.23}$$

$$A_- = S^{-1}C_A^{-1}\Lambda_- C_A S. \tag{3.24}$$

Then the split fluxes have the form $F_+ = A_+U$ and $F_- = A_-U$.

$$F_s = A_+^{\frac{L+R}{2}} U^L + A_-^{\frac{L+R}{2}} U^R. \tag{3.25}$$

The same flow state $[\frac{(L+R)}{2}]$ is used to evaluate the positive and negative Jacobians. This contrasts with the Steger-Warming scheme, in which the Jacobians are upwinded. MacCormack and Candler[34] proved that this simple modification results in a significant improvement in accuracy. This method was developed for application in boundary layers and leads to numerical instability when applied to strong shock waves. In such regions the scheme reverts back to the Steger-Warming scheme in a smooth manner with a pressure based switch described by Chandler[8].

For a higher order extension, the piecewise constant solution is replaced by a linear one, according to the relation :

$$Q(x,y)_A = Q(x_0,y_0)_A + \Phi_A \nabla Q_A \cdot \Delta r \text{ with } \Phi \in [0,1], \tag{3.26}$$

where ∇Q_A represents the constant gradient of the solution on each cell and Δr the local coordinates of a point within the element. In this expression, the parameter Φ_A is a slope limiter used to avoid a new maxima or minima. The gradients used is the same as the ones used for the viscous terms and they are described later.

The computation of the viscous terms requires the gradients of flow properties at each cell. The computation of gradients at each control volume is performed using Green-Gauss integration around the control volume boundary.[23] A weighting process[24] is used to improve accuracy so that in a regular triangular mesh made of equilateral triangles the gradient is second order accurate.

Chapter 4

Description of Monaco

This chapter gives a brief description of the DSMC code used for these simulations.

4.1 Introduction

The direct simulation Monte Carlo (DSMC) method is a numerical technique that uses particles for simulating fluid flow. The DSMC method has been successfully applied to a wide variety of rarefied gas flows. The method is based on the assumption that particle motion and collisions can be uncoupled for a time step smaller than the mean free path time between collisions. A brief description of the algorithm involves three steps. First, new particles are generated at the inflow boundaries and all particles are moved in the computational domain disregarding collisions with other particles but including interactions with wall boundaries. Each particle has its own position, mass, velocity and internal energy. The grid used has cell dimensions of the order of local mean free path in order to group possible collision partners in each cell. In the second step, a statistical method is applied to each group achieving typical collisions appropriate for the chosen time step. The models used for collisions and energy exchange are mostly phenomenological. Finally, flow properties in each cell are sampled if the calculation has reached a steady state.

4.2 Monaco

The Monaco software is split into two parts: the MONACO library, a set of subroutines for modeling the flow physics and the MONACO kernel, a set of subroutines for memory management and parallelization. The MONACO library is a collection of subroutines written in FORTRAN. These routines handle the flow physics in a single cell. The computation of particle collisions and generation of inflow particles are handled by these subroutines. Some of these sub-routines dealing with collision models and relaxation models need to be changed for different applications.

The MONACO kernel is written is C and handles the grid structure and particle management. Since this part of MONACO is completely uncoupled from the flow physics, this does not need to be changed when physical models are changed in the MONACO library. The MONACO kernel is based on unstructured triangular or quadrilateral grids. This allows for great flexibility in dealing with flows with complicated geometry and gradients. Since the CFD code also uses unstructured grids, it was straightforward to split the domain into a CFD region and a DSMC region. It also allowed for simulations using both codes to be performed on the same grids for comparison.

Particle properties are obtained from a specified distribution function at the inlet of the computational domain. Particles are paired for possible collisions. The probability of a collision is a function of the collision cross section and the densities of the species. Various techniques can be used to determine if a pair of particles collide. These include the Time Counter method,[18] the No Time Counter method,[18] and a scheme developed by Baganoff and McDonald.[33] The macroscopic collision rate must be reproduced by the instantaneous probabilities of collision. Each technique accomplishes this. However, the Baganoff and McDonald scheme is chosen for the present implemenation, because it is more computationally efficient.

The collision dynamics are performed in the center of mass reference frame. Particles may exchange translational as well as internal energy during a collision. Models for exchanging internal energy include rotational[30] and vibrational[31,32] energy. However, the present study only considers translational energy transfer, because the propellent gas is monatomic xenon. The cross sections are functions of collisional energy and depend on the mode of energy to be transferred.

In order to update the particles' positions, a time Δt must be specified. Therefore, an algorithmic approach in which a time step is used for each iteration is employed. This time step should be a fraction of the mean time between collisions in order to capture the collisional effects in the flow properly.

The collisions serve to alter the distribution function. The density, momentum, and temperature of the flow are derived from the zero, first, and second moments of the velocity distribution function respectively. Sampling the computational particles, which is essentially averaging, gives these macroscopic flow properties. For steady flows, the sampling can be extended for a large number of time steps in order to reduce statistical error. It has been shown that this error is a function of the number of particles in a cell and the number of sampling time steps.[29] For unsteady flows, care must be taken to obtain realistic averages.

The geometry may be zero dimensional to fully three dimensional. Zero dimensional simulations allow physical modeling and collisional behavior to be examined while the movement is unnecessary. A three dimensional implementation of DSMC is described in Ref.[28]. Fully three dimensional modeling requires considerably more memory and execution time than two dimensional modeling. Not only is more cell information needed, but also more particles must be employed. These two requirements lead to substantially longer simulations. Therefore, the present study assumes symmetry in the azimuthal direction and uses cylindrical coordinates. Axisymmetric flows can be represented by a two dimensional grid, but the movement routine uses all three velocity components. The geometry is assumed to be a single azimuthal plane. Particles are moved in all three directions and are then mapped back into this plane.

Particles store their positions and move through the cells according to their velocities. In the present implementation, particles which reach cell boundaries are passed to the neighboring cell. The boundaries of each cell are defined as either walls, symmetry lines, inflows, outflows, or cells which share an edge (called neighbors). Walls may be fully specular, fully diffuse, or a combination of the two. Fully specular walls simply reflect the particle back into the simulation without altering properties other than the velocity vector. Fully diffuse walls accommodate the particles to the wall temperature and sample properties from a distribution before returning them to the cell. It is often necessary to treat some of the collisions between particles and walls as specular and the rest as diffuse.[18] Symmetry lines essentially act as specular reflection walls. Particles reaching inflow or outflow boundaries are removed from the simulation. It is often important to include the facility background pressure in simulations when comparing with experimental data. The present application is a good example. To represent this effect, particles can be introduced at the boundaries at a specified density and temperature, but this may take a considerable amount of time to reach a steady state. Another approach is to impose ambient conditions uniformly in the cells at the start of a simulation and allow them to move through the domain. However, this may require substantially more particles than are desired for a simulation. A scheme which imposes a background density and temperature is described in Chapter 4. Temporary particles are created in the cells for possible collisions, but they are not tracked by the code.

Chapter 5

Hydrogen plume flow

The first step towards developing the method described for performing simulations of a complete nozzle plume system is the development and validation of a continuum code. This chapter describes the validation of the continuum code described in chapter three. The code is applied to study hydrogen plume flows in arc-jet experiments conducted at Stanford University[19]. First, the results obtained from nozzle and plume flow simulations using the continuum code are compared with experimental measurements. Detailed comparisons are also made of the plume flow results with computational results obtained from DSMC simulations. Finally the extent of validity of the continuum approach is investigated by performing a few simulations of the hydrogen gas expanding into very low background pressures.

5.1 Introduction

Low power hydrogen arc-jet propulsion devices are used in spacecraft for orbit transfer and station-keeping maneuvers. The thrust efficiencies achieved with these rockets have only reached about 30%. Many of the factors that cause this relatively low efficiency are concerned with the fluid mechanics and chemical kinetics of hydrogen. An experimental investigation employing Raman scattering to obtain number density and rotational temperature was performed at Stanford University to examine these effects at a fundamental level. Boyd has performed detailed comparisons of these measurements with results obtained from DSMC simulations[19]. The flow regime varies from low Knudsen numbers inside the nozzle to very high Knudsen numbers in the plume. These studies found that the flow is dominated by effects of thermal relaxation and by viscosity in the nozzle boundary layer. The flow conditions, availability of experimental measurements, and results from previous DSMC simulations made this system a good candidate for testing and validating the CFD code.

First, the nozzle flow simulations are performed. The domain starts at the inlet of the nozzle and ends a short distance away from the exit plane. The results obtained are validated with experimental measurements. A separate simulation of the near plume region is performed next. For this simulation the domain starts with the exit plane of the nozzle and extends into the near plume region. For these simulations the background pressure was maintained at 43Pa in the experimental facility. Detailed comparisons are made with results obtained from a DSMC code to assess the agreement between the two approaches. The computational results are compared with experimental measurements of number density and rotational temperature in the plume. After validating the CFD code, simulations of hydrogen expanding into very low background pressures are performed using the CFD code. The results obtained are compared with DSMC results to study the breakdown of the continuum approach. These flows have relatively high Knudsen numbers and test the validity of the continuum approach.

The finite volume Navier-Stokes solver can be used with unstructured triangular or quadrilateral meshes. The use of unstructured grids allows for various solution adaptive gridding techniques. In the present study, an initial solution for the flow field is obtained using a coarse grid. Grid refinement is then performed using the coarse grid solution. The solution is then transferred from the coarse grid to the fine grid. Although efficient use of unstructured grids requires further study of various solution adaptive strategies, the transfer of the coarse grid solution to the fine grid greatly reduces the time required for the final solution. Grid refinement requires an estimation of minimum cell sizes needed to capture the flow features accurately. Different methods can be used to estimate this cell size. Initially a method based on the gradient of number density, calculated from the coarse grid solution, was tried. This method ran into difficulties because the gradients were not smooth enough for the grid generator. This was avoided by generating a series of grids with cell sizes in multiples of the mean free path values obtained from the coarse grid simulation.

5.2 Experimental Details

The experiments were conducted in the vacuum facility at Stanford University.[19] The flow under consideration is the low-density expansion of molecular hydrogen from a 1kW-class NASA hydrogen arc-jet thruster. The nozzle has a throat diameter of 0.64 mm with a 20^0 degree half-angle, and an exit-to-throat area ratio of 225:1. The mass flow rate through the thruster is 14.1 mg/s and the stagnation temperature is 300K. The conditions chosen for examination represent a cold flow configuration in which the arc is not ignited. These conditions correspond to a Knudsen number of the order of 0.01 at the nozzle exit.

The flow is assumed to expand into a background pressure of 43 Pa. The overall experimental configuration is shown schematically in figure 5.1. Of particular

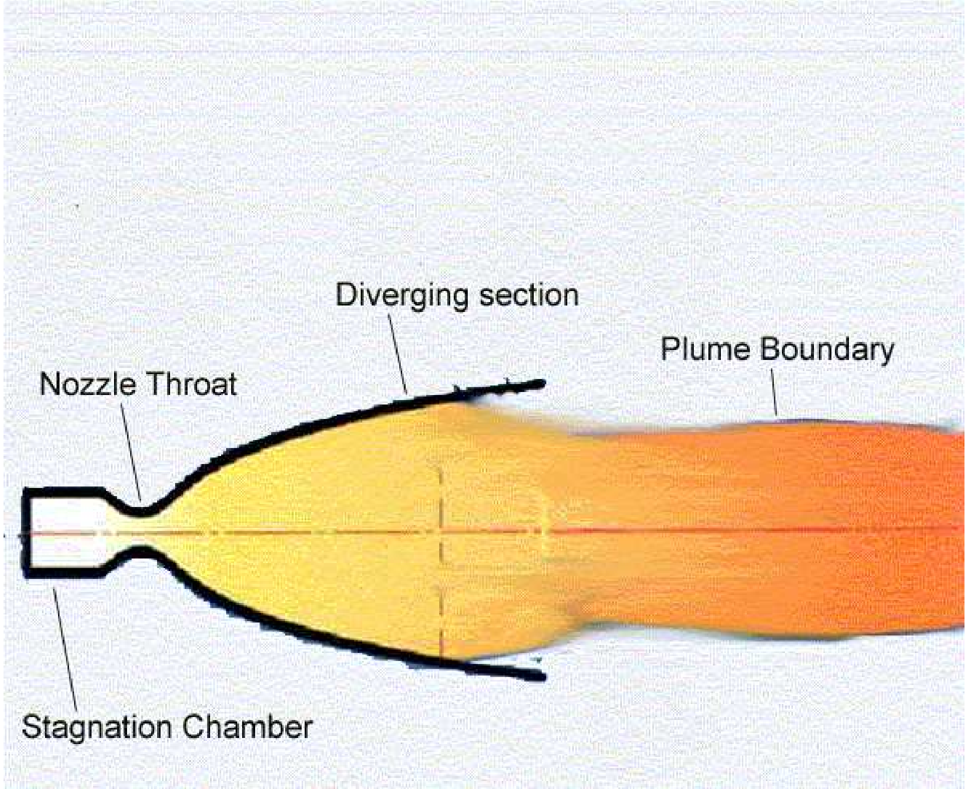

Figure 5.1. Schematic of the experimental system

interest is the position of the vacuum pumps with respect to the expanding flow. The location of the pumps will clearly give a non-symmetric pressure distribution. It is difficult to perform an exact simulation of the chamber residual pressure since it is not distributed homogeneously throughout the chamber.

The experimental measurements employ spontaneous Raman scattering. Raman scattering is an inelastic, linear two-photon scattering process. An incident photon scatters off an H_2 molecule causing a change in the molecular quantum state and a corresponding change in the energy of the scattered photon. The number of scattered photons is linearly proportional to the number of incident photons and the density of the scattering species. Density is determined by the absolute intensity of all transitions combined in conjunction with the signal from a reference cell. For the present comparisons the experimental data, taken along the plume centerline, give the density of the J=1 rotational state. The J=1 rotational state was chosen in order to facilitate high spatial resolution. Each experimental data point is obtained over a volume that is 4mm in length axially and 0.1mm in the radial direction. The relative intensity of the various transitions can be used to determine a rotational temperature, assuming partial thermodynamic equilibrium exists among the rotational states. Experimental data is taken along the exit plane and the plume centerline.

5.3 CFD Code

A description of the Navier-Stokes solver is presented in chapter three. A kinetics model and the boundary conditions need to be implemented before the code is applied to a specific study. This section describes the details of the kinetics model and the boundary conditions implemented for this particular application.

5.3.1 Kinetics

The problem under consideration is a single species flow of molecular hydrogen. The stagnation temperature of the flow is 300K. Since the temperatures involved are low, the vibrational mode is assumed to be frozen and dissociation of hydrogen is not important. Model parameters for the rotational relaxation rate and the viscosity coefficient of molecular hydrogen must be provided as inputs to the code. The kinetics scheme implemented in the code is based on a model developed for DSMC simulations of such flows by Boyd et al[19]. The viscosity model used has a temperature coefficient of 0.67 and gives an excellent fit to measured data[19]. For the CFD simulations, the energy exchange rate between the translational mode and the rotational mode is given by

$$Q_{t-r} = \rho \frac{e_r^*(T) - e_r}{\tau_r} \tag{5.1}$$

where $e_r^*(T)$ is the rotational energy per unit mass evaluated at the local translational temperature and τ_r is the relaxation time. For these simulations, the relaxation time is based on the form

$$\tau_r = \tau_c * Z_r \tag{5.2}$$

where τ_c in the inverse of the molecular collision rate. τ_c is calculated using

$$\tau_c = \pi\mu/(4p), \tag{5.3}$$

where μ is the coefficient of viscosity and p is the pressure[20]. Z_r is the rotational collision number for hydrogen which is given by[19]

$$Z_r = 10480/T^{\omega} \tag{5.4}$$

ω, the temperature coefficient of viscosity, is assumed to be 0.67.

5.3.2 Boundary Conditions

The two separate simulations require slightly different boundary conditions. For the nozzle simulations, the inlet boundary conditions are subsonic and exit boundary conditions are supersonic. The nozzle wall is assumed to be isothermal.

For the plume simulations, the solution domain starts at the exit plane of the nozzle. There are three types of boundaries corresponding to the exit plane of the nozzle, outflow boundary and the axis of the plume. The inlet is supersonic and so all the conditions are prescribed at the beginning of the simulation and not changed. These inlet conditions, which correspond to the conditions at the nozzle exit, are obtained from a DSMC simulation of the nozzle flow. De-coupling the nozzle flow simulations from the plume simulations saves a great deal of computational expense. The decoupling approach has been successfully applied in previous investigations using the DSMC technique by Boyd et al[25] and Penko et al[26] .

The outflow boundary condition depends on the Mach number of the flow normal to the domain exit plane. If the flow is supersonic all the flow properties are extrapolated from the flow domain. If the flow is subsonic the pressure at the eexit is assumed to correspond to the background pressure of the flow and all other flow properties are extrapolated or calculated. The axis is assumed to be a line of symmetry. The domain is made large enough so as to minimize the effect of the exit boundary conditions on the flow near the nozzle exit.

5.4 Nozzle Simulation Results

First, the CFD code is validated for nozzle simulations. The CFD results obtained are compared with experimental measurements. Figure 5.2 shows the comparison of number density of the J=1 rotational state of hydrogen in the nozzle exit plane. The number density of the excited state is calculated using the equilibrium expression along with the number density and the rotational temperature obtained from the simulation. There is reasonably good agreement between numerical and experimental results. Figure 5.3 shows the rotational temperature across the nozzle exit plane. The agreement between the numerical results and the experimental measurements is very good.

To check the sensitivity of the solution to the resolution of the grid, the simu-

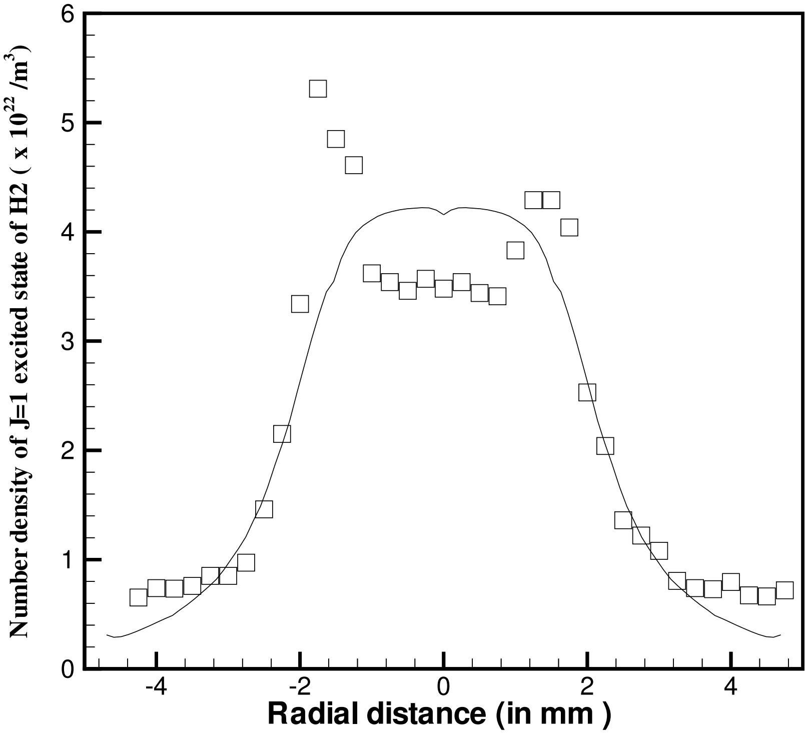

Figure 5.2. Comparison of measured and calculated data for the density of the (J=1) rotational state across the nozzle exit plane

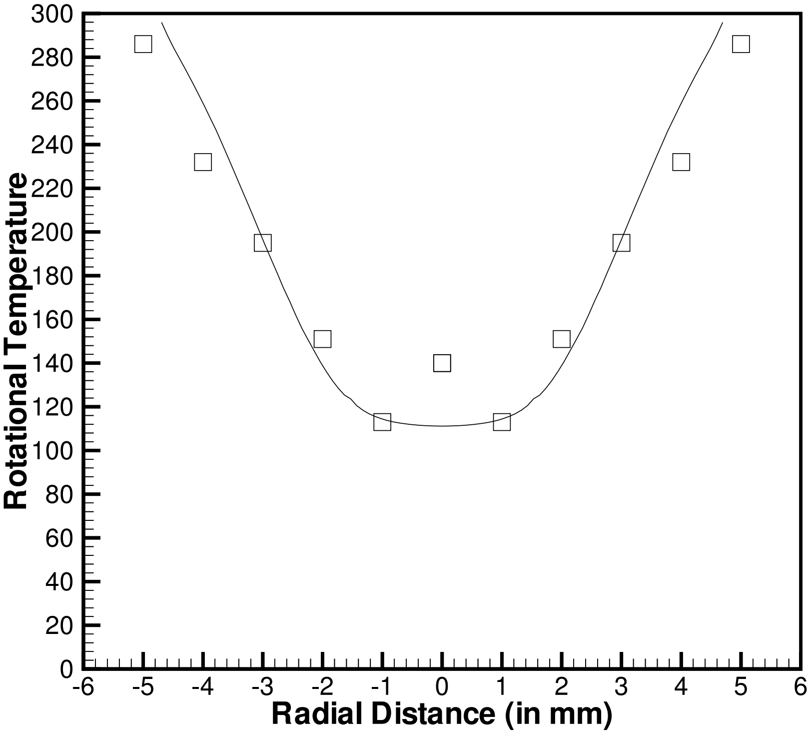

Figure 5.3. Comparison of measured and calculated data for the rotational temperature across the nozzle exit plane

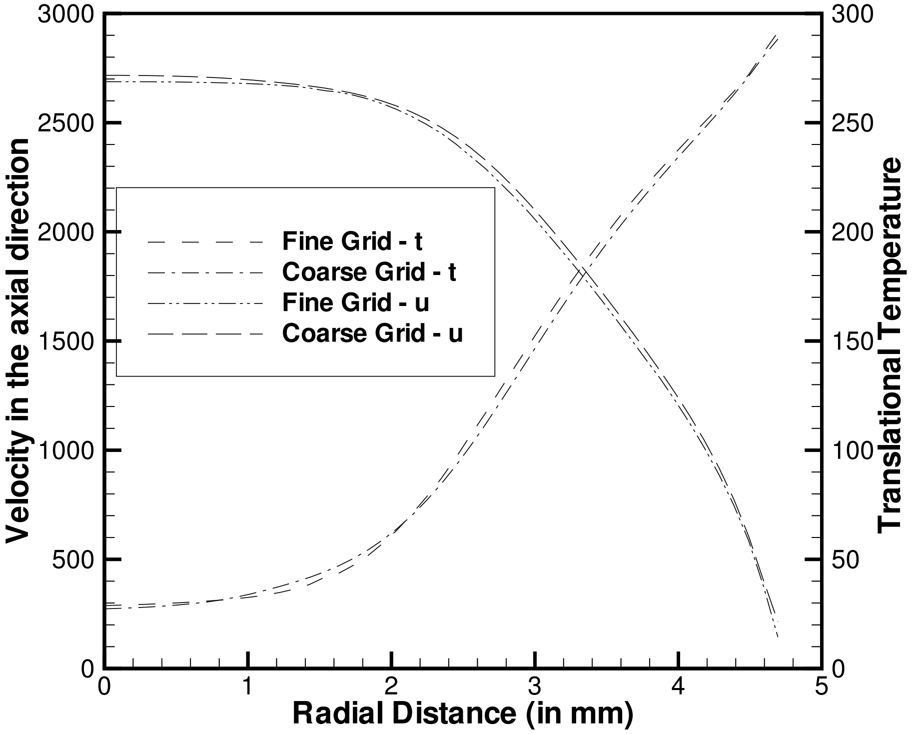

Figure 5.4. Comparison of axial velocity and translational temperature along the nozzle exit plane computed with CFD method using different grids

lations are repeated on a finer grid. The coarse grid has around 10,000 cells while the fine grid has about 36,000 triangles. There was no appreciable difference between results from the two simulations. Figure 5.4 shows the comparison of the velocity in the axial direction and the translational temperature along the axis obtained using different grids. Thus it can be concluded that grid resolution is not an important issue for these flows.

5.5 Plume Simulation Flow field results

Plume flow field properties predicted by the CFD code are presented in this section. The flow domain begins at the exit plane of the nozzle and extends to about 10 cm in the axial direction and 3 cm in the radial direction. Contours of the number density in particles per m^3 obtained for this condition are shown in Figure 5.5. The finite back pressure creates a thin jet of diameter about 1 cm. The flow is highly overexpanded and shows a very complicated flow pattern involving Mach disks and shock waves. Contours of Mach number are shown in Figure 5.6. The supersonic portion of the flow is restricted to a narrow core of diameter 8mm and is enveloped by a barrel shaped shock structure. There is a region of high density between the shock and the plume boundary where the flow is decelerated rapidly.

The flow shows a repetitive pattern of expansion followed by compression, which decreases in strength as we go downstream. The pressure distribution along the axis, shown in Figure 5.7, clearly shows the extent of overexpansion and the repetitive pattern of expansion and compression. The amplitudes of these compressions are found to depend very highly on the cell size. Figure 5.8 shows the number density along the plume centerline obtained using different grids. Results using three

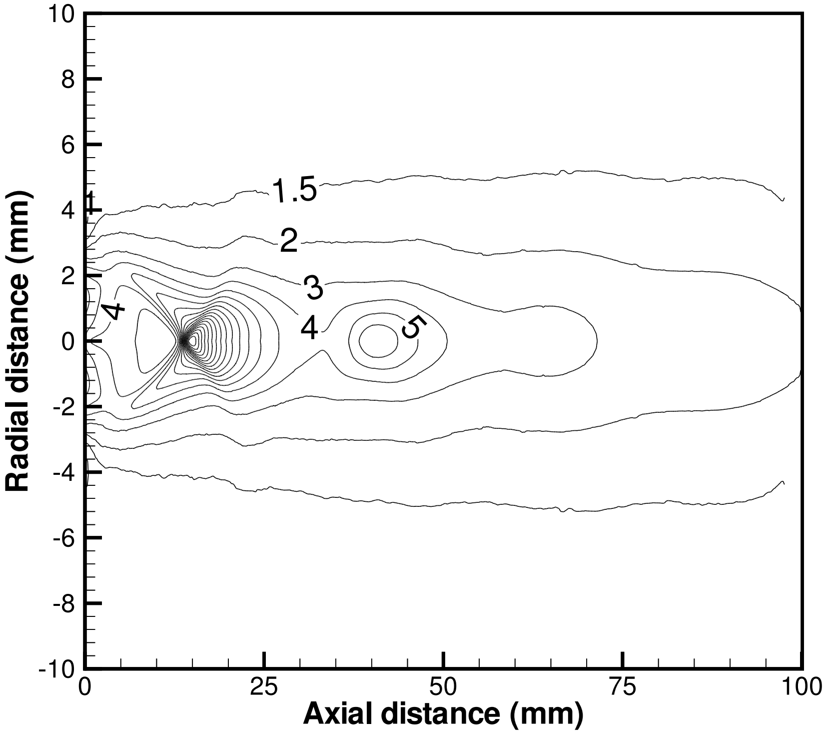

Figure 5.5. Contours of number density in molecules m^{-3} computed with CFD method at a background pressure of 43 Pa.(contours multiplied by 10^{22})

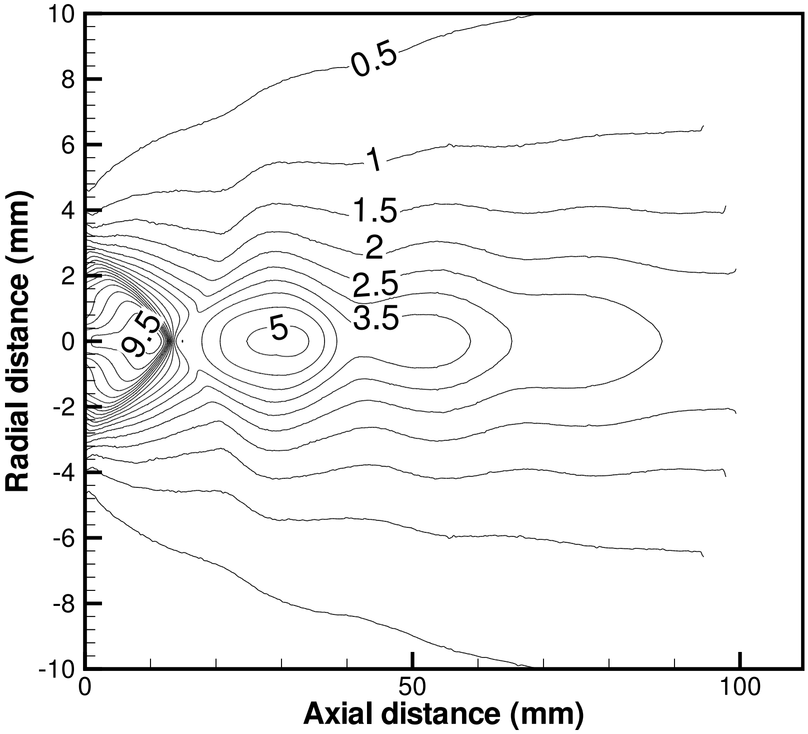

Figure 5.6. Contours of Mach number computed with CFD method at a background pressure of 43 Pa.

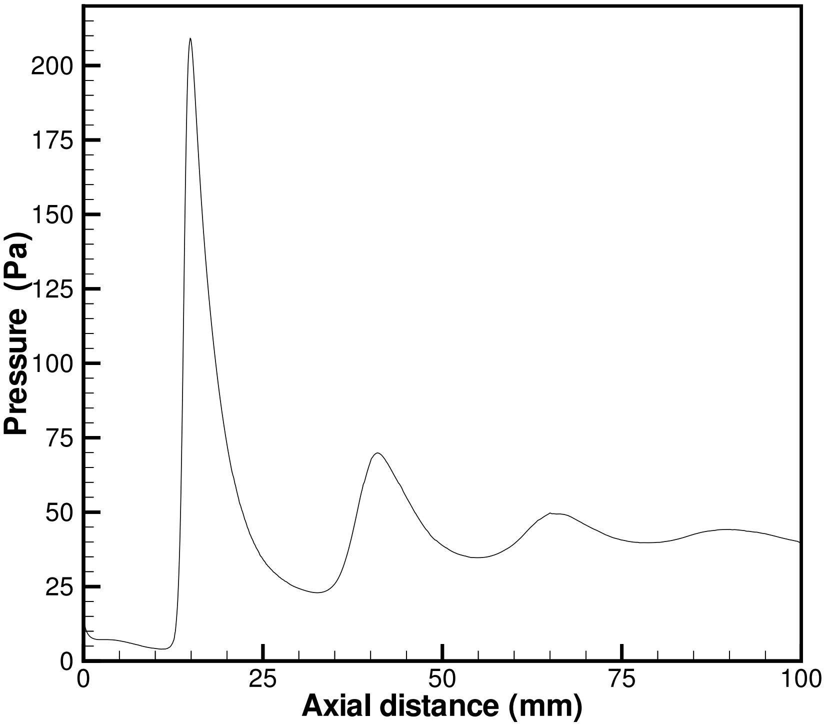

Figure 5.7. Pressure along the plume centerline computed with CFD method at a background pressure of 43 Pa.

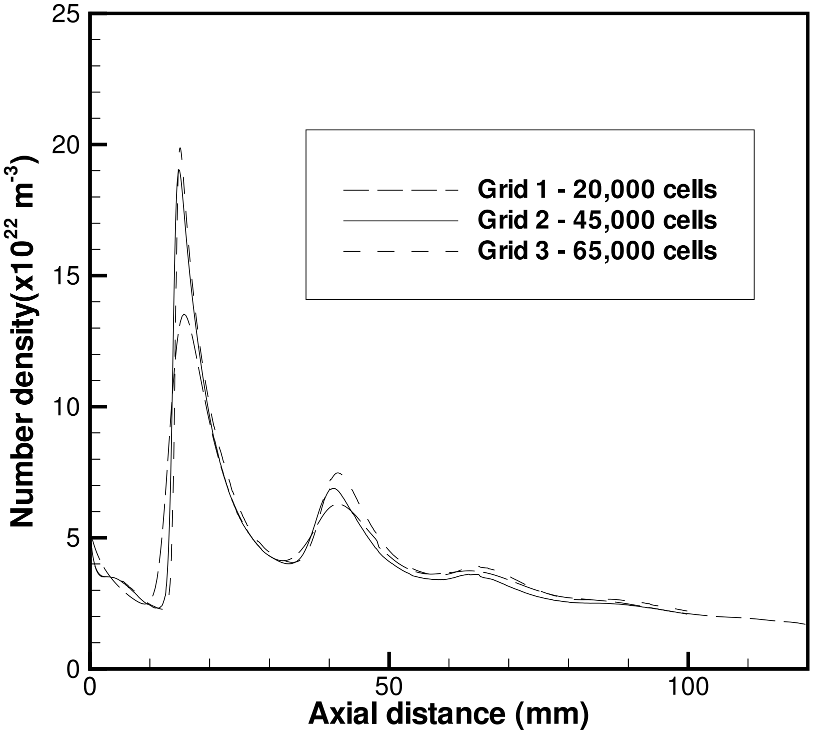

Figure 5.8. Comparison of number density along the plume centerline computed with CFD method at a background pressure of 43 Pa using different grids

grids are shown in the figure. The coarsest grid has 20,000 cells. The solution obtained using this grid is used as a basis for generating other grids. The other grids have 45000 and 65000 triangles respectively. As the cell size is decreased the amplitude of the waves increases. Due to efficiency considerations, only the first compression is captured in a grid independent manner. In this region the solutions from the two fine grids coincide. Thus it can be concluded that in this region the solution is more or less free of grid effects. Further refinement, even in other regions does not effect the solution in this region. The complex nature of the flow and the need for extremely small cells to capture the flow accurately underlines the advantages of flexible gridding techniques available with unstructured grids.

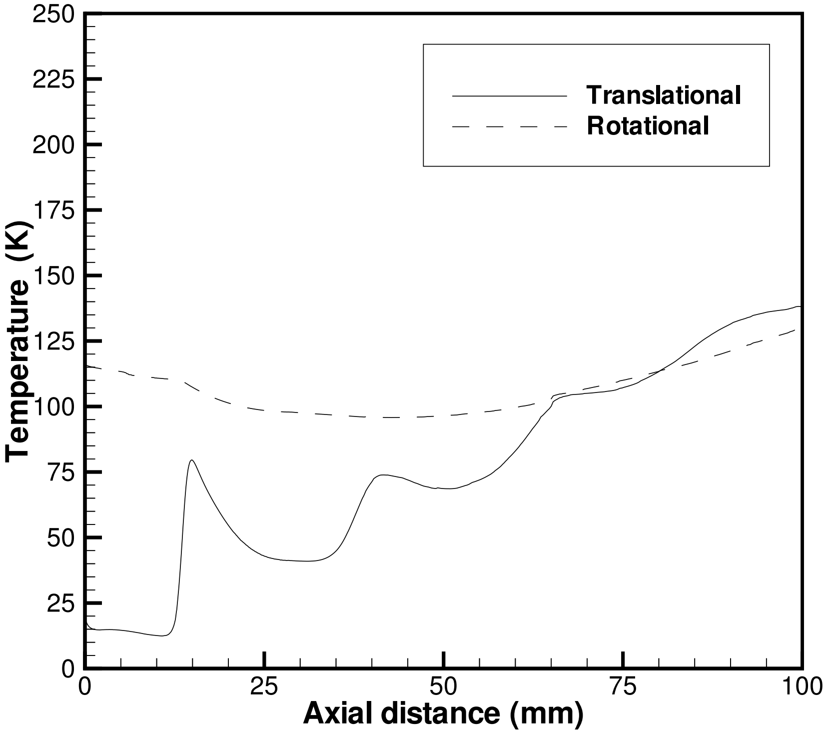

Figure 5.9. Translational and rotational temperature along the plume centerline computed with CFD method at a background pressure of 43 Pa.

There is a high degree of rotational non-equilibrium in the flow. Figure 5.9 shows the rotational and translational temperatures along the plume centerline. Due to the rapid expansion in the nozzle the translational temperature is much lower than the rotational temperature at the exit of the nozzle. Inside the plume near the axis, the translational temperature rises due to a series of rapid compression processes and becomes higher than the rotational temperature. Far downstream both temperatures approach equilibrium as the strengths of these compressions decreases.

5.6 Comparison with DSMC Results

This section presents the results obtained from the DSMC simulations and their comparison with the results from the CFD computation. The DSMC code used is described in chapter four. The code is used with unstructured triangular grids. The DSMC simulations are carried out using the same grid as the CFD simulations. The grid consists of about 42,000 triangles. The cell sizes in the region near the nozzle exit are about three times the mean free path. The CFD simulations are performed on a SGI workstation and take around 30 hours of CPU time to converge. The DSMC computations are carried out on an IBM SP2. The code is run in the parallel mode using 4 processors for about 12 hours. For these simulations there were about one million particles in the simulation.

The exit plane boundary conditions for the DSMC simulation requires knowledge of both pressure and temperature. The pressure is assumed to be the residual chamber pressure of 43 Pa. The temperature cannot be calculated a priori and there are no experimental measurements available. Thus for the purpose of these

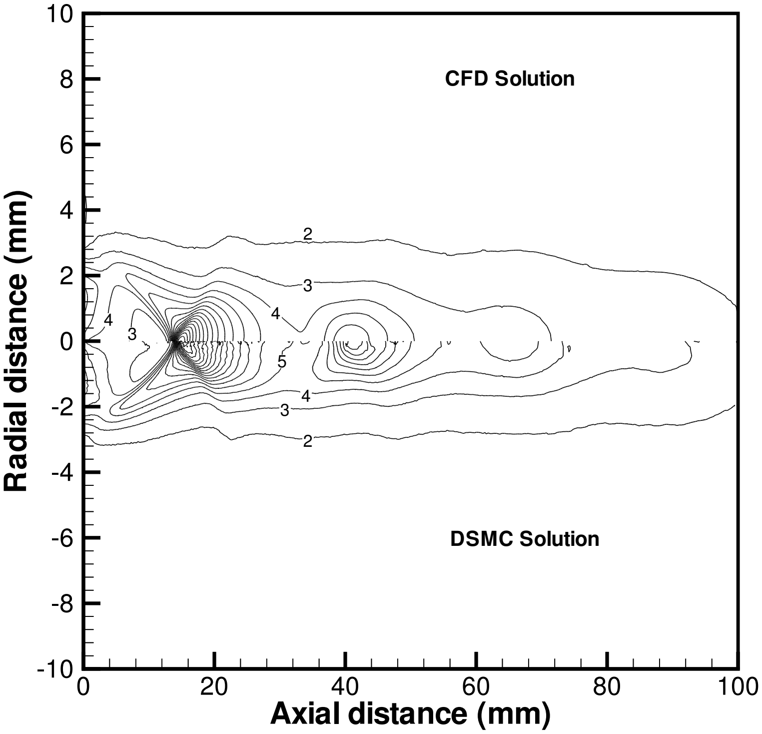

Figure 5.10. Comparison of contours of number density in molecules m^-3 computed with the CFD method and DSMC method at a back pressure of 43 Pa.(contours multiplied by 10^{22})

simulations the exit plane temperature are taken from the CFD simulations. Previous results had indicated that the temperature at the exit plane boundary does not effect the flow near the nozzle exit, which is the primary region of interest.

First, number density contours are compared to assess the overall agreement. From Figure 5.10 it can be concluded that both methods give very similar results. The flow properties along the axis are then compared in detail. Figure 5.11 shows the number density profiles along the plume centerline in the axial direction. There is very good agreement between the two solutions for about 4 cm in the axial direction. The amplitude of the secondary compression region is under-predicted

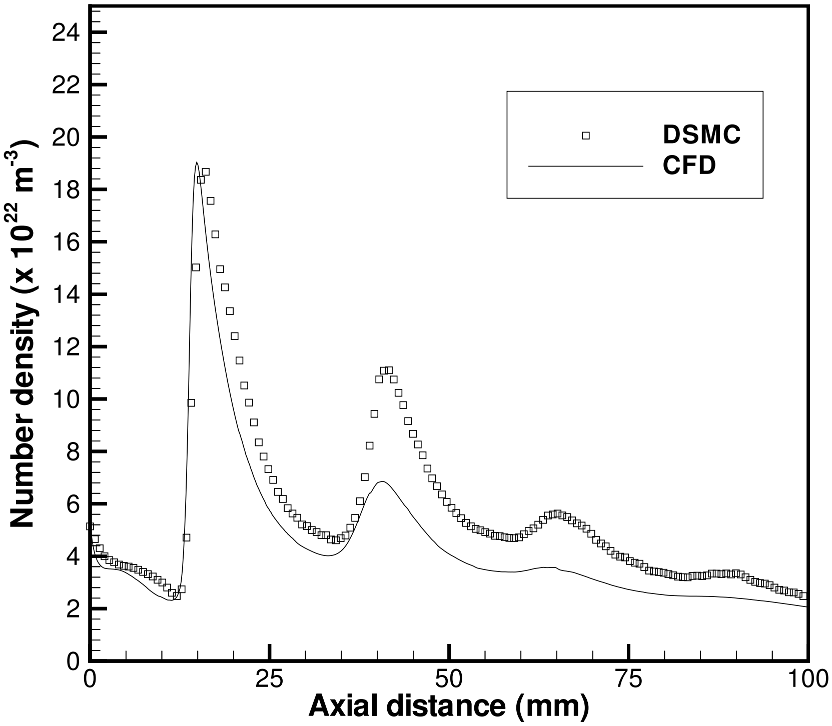

Figure 5.11. Comparison of number density along the plume centerline computed with the CFD method and DSMC method at a back pressure of 43 Pa.

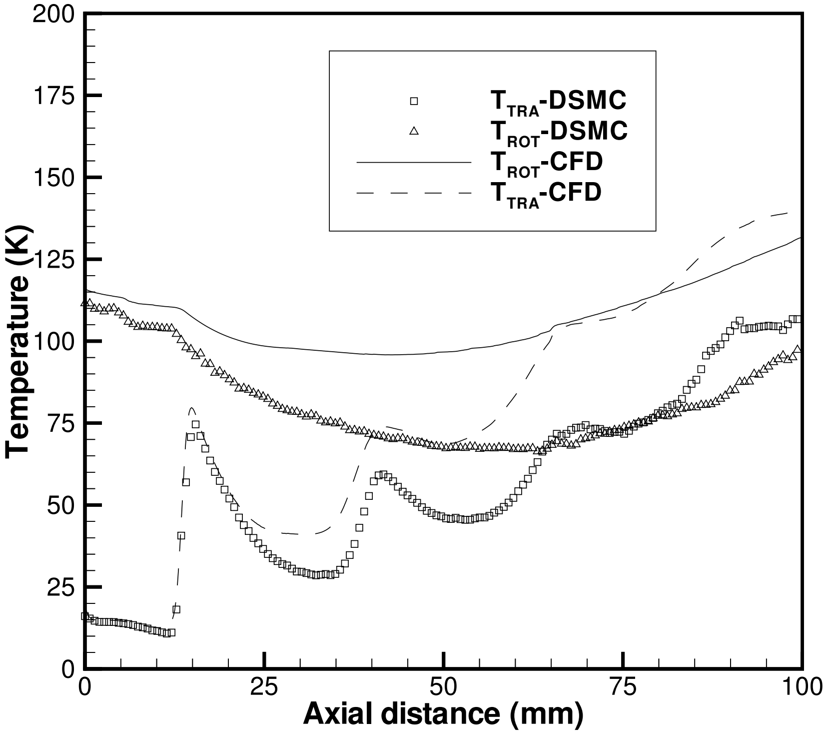

Figure 5.12. Comparison of temperatures along the plume centerline computed with the CFD method and DSMC method at a back pressure of 43 Pa.

by the CFD code. This is because the grid resolution there is not sufficient for the CFD method.

Figure 5.12 shows the temperature profiles along the axis. For clarity, while plotting the DSMC results only one in three data points is shown. The translational temperature shows very good agreement throughout the first expansion and compression. The results start to differ where the cell sizes increase and the lack of resolution decreases the accuracy of the CFD results. The rotational temperature predicted by the CFD simulation is consistently higher than the DSMC results. Given the complex non-equilibrium nature of the flow, this is not surprising. This behavior is not investigated in detail because its influence on other flow properties

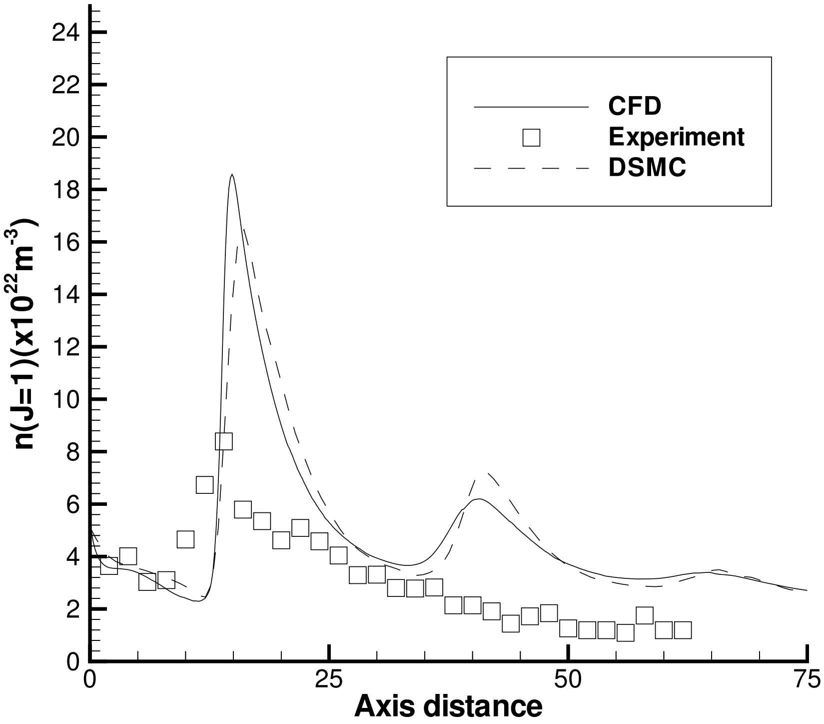

Figure 5.13. Comparison of number density along the radial direction at a axial distance of 1cm computed with the CFD method and DSMC method at a back pressure of 43 Pa.

is minimal and the focus of this investigation is not on accurate modeling of the rotational relaxation process.

Figure 5.13 shows similar comparisons for number density along a straight line in the radial direction at a station located at a distance of 1 cm along the axis. Figure 5.14 shows comparisons for temperatures performed in the radial direction at the same location. Since this region has sufficient grid resolution the agreement is in general very good.

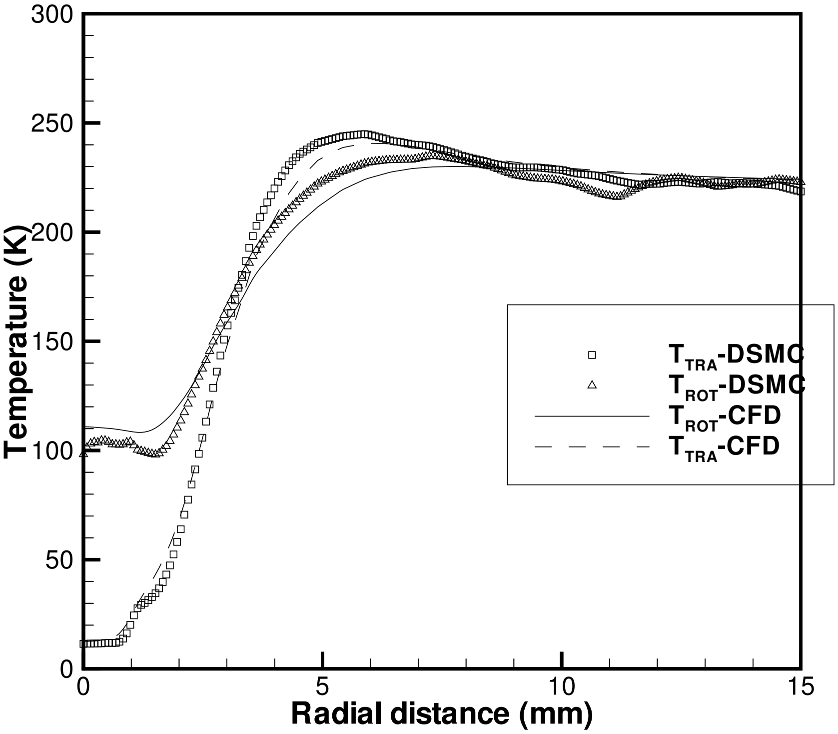

Figure 5.14. Comparison of temperatures along the radial direction at a axial distance of 1cm computed with the CFD method and DSMC method at a back pressure of 43Pa

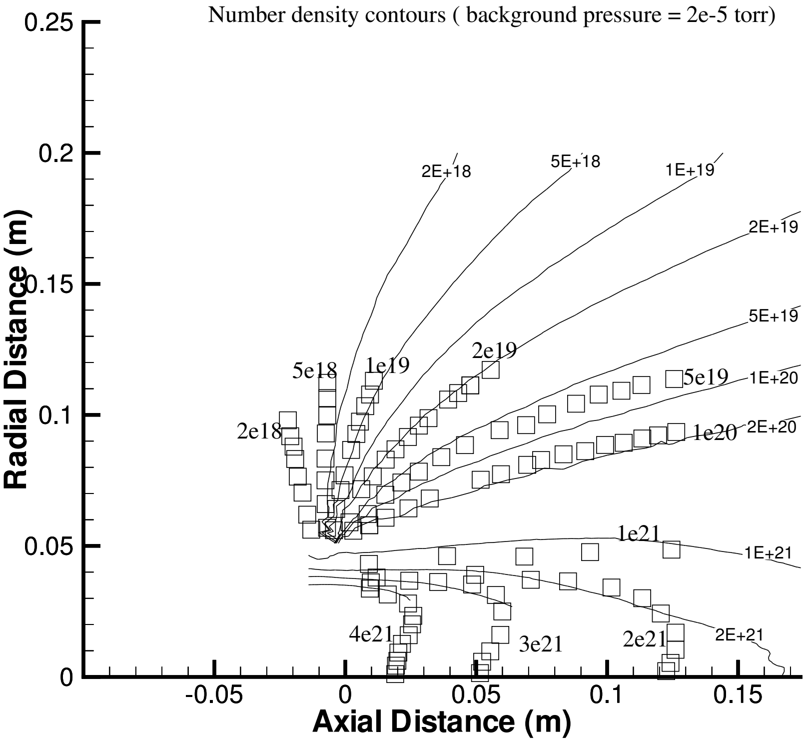

Figure 5.15. Comparison of measured and calculated data for the density of the J = 1 state along the plume centerline at a back pressure of 43 Pa.

5.7 Comparison with experimental data

This section presents the comparison of the numerical results with the data from experimental measurements.

For the numerical results, the number density and the rotational temperature obtained from the simulation are combined using the usual equilibrium expression to calculate the number density of the rotationally excited state. Figure 5.15 shows the comparison between the two numerical results and the experimental data. For the first 10 mm the agreement between the numerical solutions and the experimental data is very good. The shock like structure starts around 2 to 3 mm closer to the nozzle exit in the experimental data compared to the numerical results. This could be because of the uncertainty in the spatial distribution of the prescribed back pressure. A small increase in the back pressure prescribed for the numerical simulations would move the shock upstream. The validity of the equilibrium expression used for calculating the excited state number density is also questionable.

Given these uncertainties the agreement is very good. The experimental measurements do not have enough resolution to make an accurate estimate of the peak of the number density distribution. The numerical results also show a much more pronounced secondary compression region. Since the flow field exhibits features with length scales of a millimeter, more high-resolution experimental results are required for a more detailed study.

The experimental results reach the free stream number density at a shorter distance from the nozzle exit. In the CFD simulations a pressure-based boundary condition is used. This is chosen because of its simplicity and also because it has been used for earlier studies. The uncertainty in the chamber pressure, coupled with the difference in free stream number density suggests that a number density based boundary condition is more appropriate for comparison with these experimental measurements. Using the measured values of the excited state number density and the numerical results for the rotational temperature, the number density at the domain exit can be back calculated and a new simulation could be performed with a number density based boundary condition. However it is very difficult to specify boundary conditions that accurately represent plume expansion in a vacuum chamber

5.8 Low back pressure simulations

To estimate the extent of validity of the continuum approach, simulations are carried out for two further cases involving very low back pressures. In this section, the comparison between those results and the results obtained from DSMC simulations are presented.

First results from simulations with a back pressure 10 Pa are compared. Figures 5.16 and 5.17 shows the number density and temperature along the plume centerline for this case. For the first 3 cm the agreement is very good, similar to the 43 Pa case. It can be observed that the shock like structure has moved downstream and its strength has also decreased. The location of the shock like structure is closer to the nozzle exit in the CFD simulation. This could be because of poor grid resolution. Comparisons performed along a radial line at a distance of 1cm along the axis (not shown) give very good agreement between the two solutions. Although the final results indicate that the CFD code can be used for such low back pressures it was significantly more difficult to get the code to converge for this case in comparison with the 43 Pa case.

Finally, CFD results for the plume expanding into a back pressure of 1 Pa are compared with DSMC results. Figure 5.18 shows the number density and Figure 5.19 shows the temperatures along the plume centerline. In this case the flow resembles a plume expanding into vacuum. The shock like structures found in the previous flow field solutions, are not visible here. The agreement between the CFD results and DSMC results is still very good. The slight disagreement in the rotational temperature in spite of the excellent agreement in the translational temperature suggests that the disagreement in rotational temperature seen even

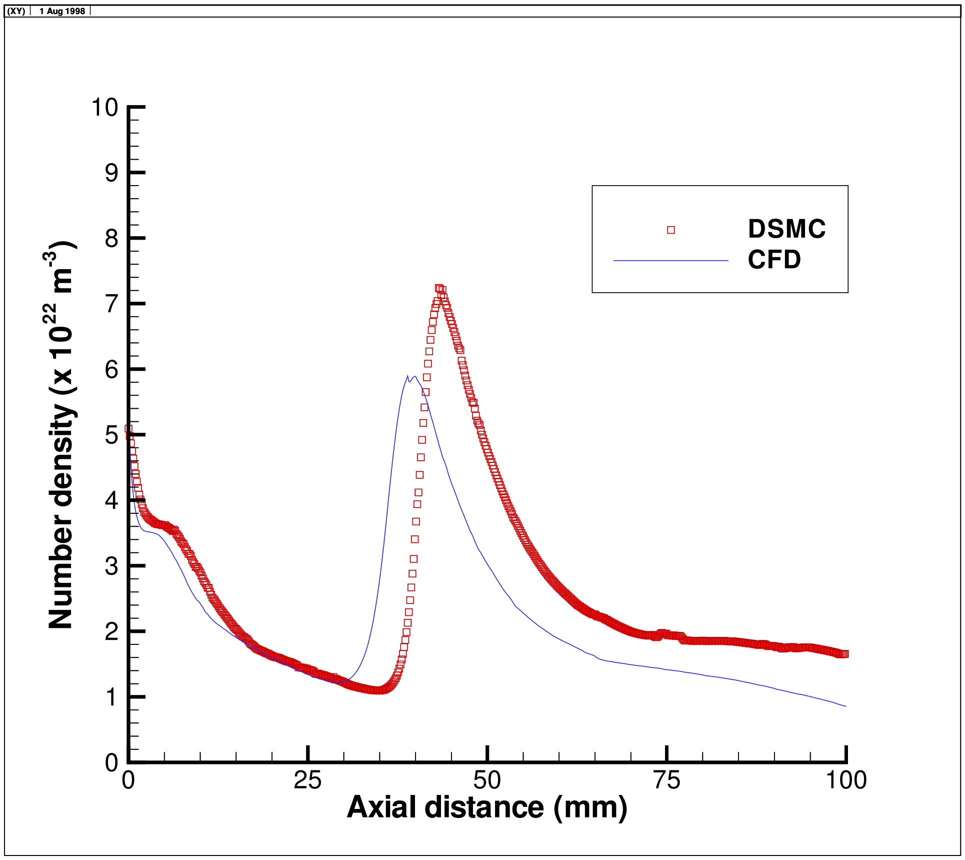

Figure 5.16. Comparison of number density along the plume centerline computed with the CFD method and DSMC method at a back pressure of 10 Pa.

in the previous simulations is not due to rotational relaxation effects. The CFD code seems to be able to predict the expansion region very well. Like the previous case it was very difficult to obtain the converged solution.

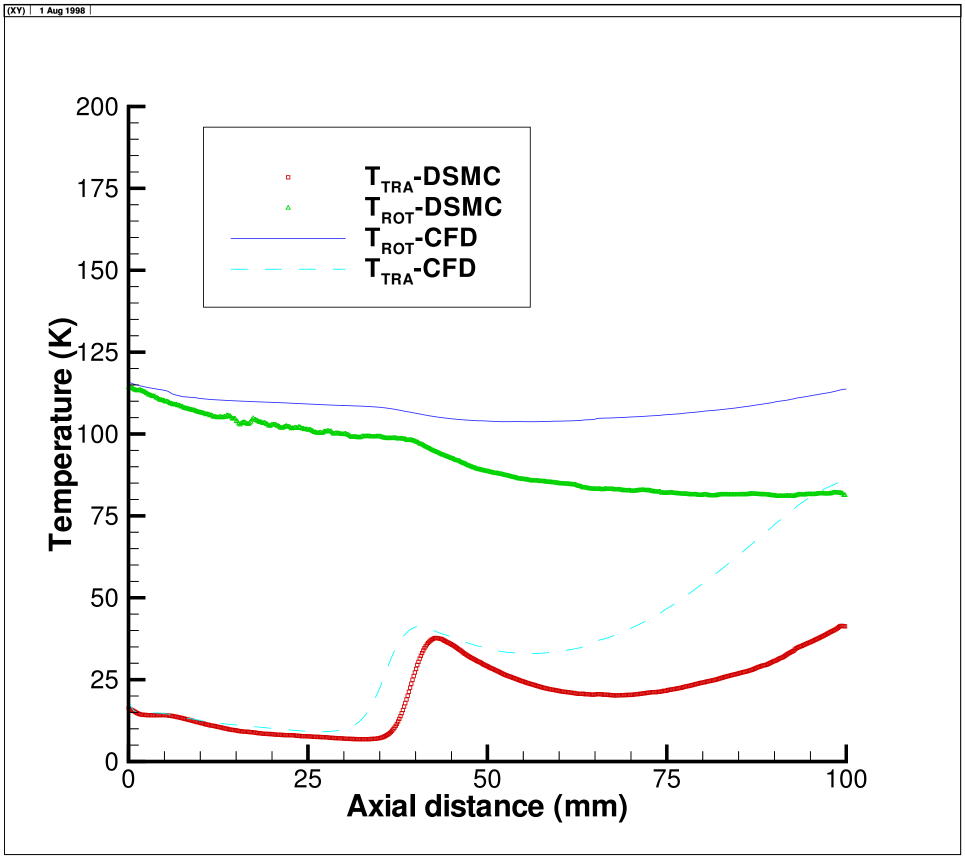

Figure 5.17. Comparison of temperatures along the plume centerline computed with the CFD method and DSMC method at a back pressure of 10 Pa.

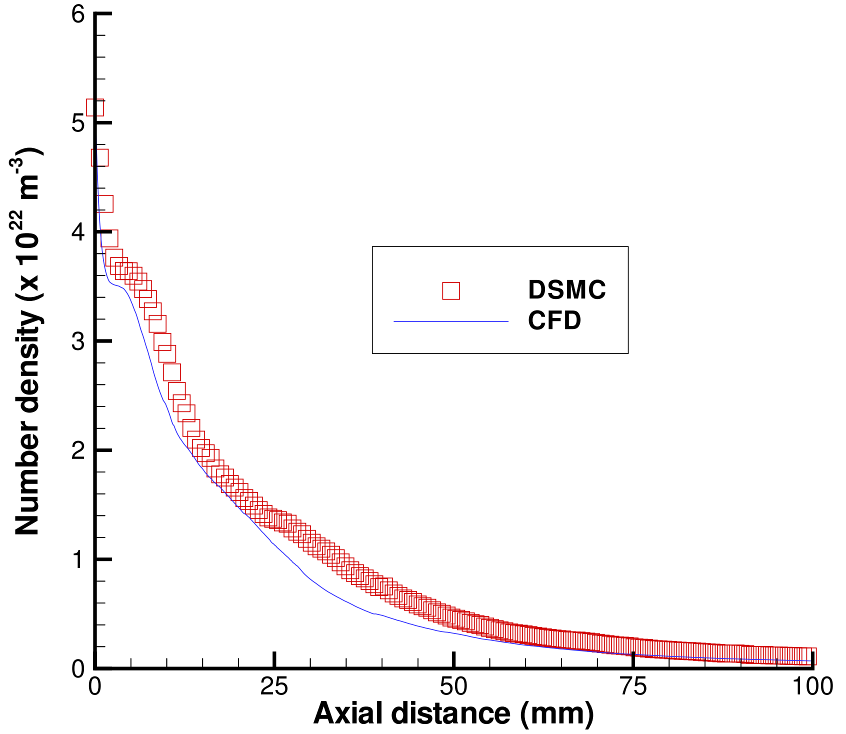

Figure 5.18. Comparison of number densities along the plume centerline computed with the CFD method and DSMC method at a back pressure of 1 Pa.

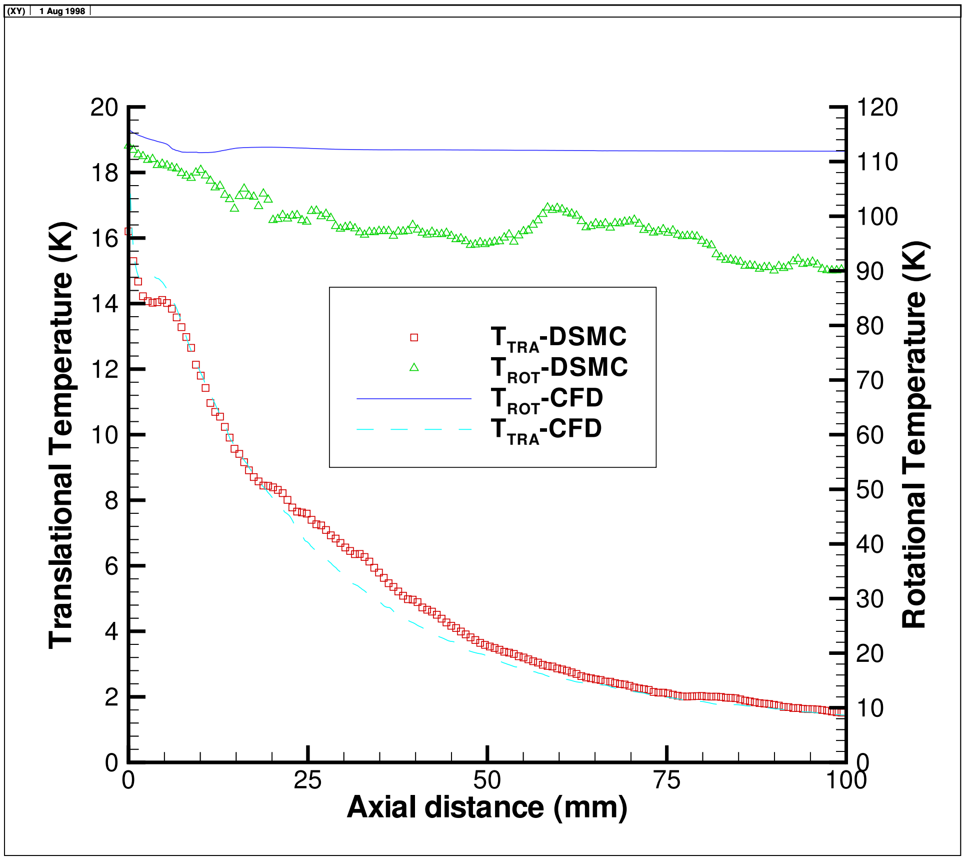

Figure 5.19. Comparison of temperatures along the plume centerline computed with the CFD method and DSMC method at a back pressure of 1 Pa.

5.9 Conclusions

An upwind finite volume code for solving the Navier-Stokes equations on unstructured triangular grids was developed. A kinetics model for hydrogen consistent with a previously developed DSMC model was implemented. It was successfully applied to investigate low-density hydrogen plume flows. This completes the validation of the CFD code, which was the primary motivation for this study.

The two numerical results were found to be in good agreement with each other. This validates the use of CFD codes as an efficient alternative to DSMC methods for performing such flow simulations. The comparison between the numerical results and experimental measurements was found to be good in terms of overall flow features. For a more detailed quantitative comparison higher resolution experimental measurements are required. The experimental measurements could not be used to differentiate between the two computational methods. An assessment of the validity of some of the equilibrium relations used for data reduction also needs to be performed.

An important conclusion of this study is that these solutions exhibit a high degree of grid dependence. This was found to be true of both the DSMC and CFD computations. Thus care should be taken to ensure that the grid resolution is fine enough to obtain accurate results. This emphasizes the importance of flexible gridding techniques provided by the use of unstructured grids. For this system, it is difficult to separate the results of the grid dependence from the physics of the problem. An exhaustive grid independence study was not carried out since it would not add to our understanding of the flow. Further refinement of the grid did not improve the agreement with the experimental measurements.

From the above computations it can be concluded that, from the point of view of application of CFD methods, these rarefied flows can be roughly divided into three regimes. In the first regime, the back pressures are high enough to make the application of CFD methods more efficient than particle based methods. In the second regime, CFD methods can be applied but the difficulty in obtaining a solution makes DSMC methods much more attractive. Presumably there is a third region where the continuum approach breaks down and the CFD solutions if obtainable would disagree with the DSMC results.

The main limitation of using this system for testing the combined approach is that we could not clearly demonstrate the third region. Since DSMC simulations could be performed for the nozzle itself, this system did not allow for a clear demonstration of the need for the continuum approach. Thus a system with different flow conditions and more detailed experimental measurements is required to clearly demonstrate the advantages of the combined methodology and the breakdown of the continuum approach. The following chapters present simulations of a carbon dioxide expansion flow that does not have these limitations.

Chapter 6

Computation of the CO2 Nozzle flow

6.1 Introduction

This chapter and next two chapters present the details of a complete nozzle plume simulation carried out by using the combined CFD DSMC methodology described in chapter two. This chapter presents the simulations of the nozzle flow and comparisons with experimental measurements. The CFD code is applied to study carbon dioxide expansion into hard vacuum. The results are compared with experimental measurements made at Arnold Engineering Development Center (AEDC)[9].

An accurate assessment of plume impingement issues requires detailed understanding of the fluid dynamics and kinetics of the nozzle flow and plume flow. With this in mind, several experimental and numerical studies were directed towards the prediction and characterization of such flows. One such study was an experimental test program instituted by the Air Force Rocket Propulsion Laboratory (AFRPL) and performed in 1985 at the Arnold Engineering Development Center (AEDC). The basic objective of that study was to define flow characteristics of pure-gas expansions into hard vacuum by obtaining a comprehensive database that could be used to validate computational codes. The results from this study, previously classified, are now available in the open literature.[9] This represents the first attempt to make detailed comparisons of these measurements with numerical computations.

Computer simulations are performed for the complete system from the inlet of the nozzle to the outer plume regions. This chapter presents the results from the CFD simulation of the nozzle flow and near plume region. These results are compared with experimental measurements made by Bailey. Flow field results in the plume region, an analysis of breakdown of continuum and results from the simulation of the backflow region will be presented in the subsequent chapters.

6.2 Experimental Details

This section describes the experimental setup, the nozzle conditions and gives some details of the configuration chosen for numerical investigation. The experiments was described in detail by Bailey.[9]

6.2.1 Test facility

The experimental program was conducted in a 4 by 10 feet research vacuum chamber (RVC) at the AEDC. The RVC is a stainless steel cylindrical vacuum chamber with an internal diameter of approximately 3.5ft and an overall length of approximately 14ft. Vacuum conditions within the RVC are achieved through the use of mechanical pumps, diffusion pumps and LN_2 cryopumps. A number of basic investigations of various low-density phenomena were carried out at this test facility. A wide range of flow diagnostic techniques was used to determine the characteristics of the plume. The effects of nozzle area-ratio, lip geometry, chamber pressure, condensation, and cryopumping in the nozzle backflow region on the characteristics of the plume were among the issues investigated.

6.2.2 Choice of nozzle and gas supply

The design of the test nozzles and the choice of the test gas took into account the requirements of the test program, the operational characteristics of the RVC and the results of earlier studies conducted in the RVC. CO_2 expansions were studied because they allowed the use of inexpensive LN_2 cryopumping as opposed to N_2 expansions which would have necessitated the use of more expensive GHe cryopumping. Earlier studies showed that acceptable background pressures (10^{-5} torr) could be achieved with nozzle flow rates of the order of 2 gm/sec. To simplify nozzle design and fabrication, the study was limited to 15-degree half-angle conical configurations with a fixed exit diameter of 4" and various throat diameters.

The evaluation of the mechanism affecting the flow of gas into the nozzle backflow region was an area of prime interest in the experimental study. It is generally accepted that this gas flow derives from the expansion of the nozzle boundary layer. Therefore, one of the requirements of the study was that the nozzle boundary layer should be of sufficient thickness to permit spatially resolved flow field measurements. The number density on the exit-plane centerline should be of the order of $10^{15}/cm^3$ in order to minimize the magnitude of the quenching corrections required for electron beam fluorescence measurements. The stagnation temperature of the gas should be controlled such that condensation in the expanding flow would occur downstream of the nozzle exit plane. With these constraints in mind, nozzle stagnation conditions and throat diameter were chosen so as to produce an acceptable flow at the nozzle exit plane.

Three nozzles with corresponding operating conditions were used for the experimental study. As a first attempt at detailed numerical analyses of these experiments it was decided to choose one nozzle and study it in detail. Since the focus of this investigation is more on the CFD aspect of these simulations, the configuration with the maximum number of measurements in the continuum and near continuum region is chosen.

This configuration involves a nozzle with a throat diameter of 0.6” and area-ratio of 44.4. The stagnation temperature of the flow is 710K while the stagnation pressure is 36.5 torr. The massflow rate through the nozzle was maintained at 1.77 ± 0.06 gm/sec. The numerical results are compared with pitot pressure measurements along the plume centerline, flow angle measurements in the plume, and electron beam fluorescence measurements of number density and rotational temperature along the radial direction at a few axial stations. The objective of these comparisons is to assess the validity of the numerical data and the accuracy of the measured data.

6.3 CFD Computations

Similar to the previous study, a few modifications have to be made to the code to perform simulations of carbon dioxide expansions. This section presents the details of the kinetics model and the details of the boundary conditions that are specific to this application.

6.3.1 Kinetics model for CO_2

Carbon dioxide is linear tri-atomic molecule. It has three translational degrees of freedom, and two rotational degrees of freedom. The characteristic temperatures for the first three vibrational modes of carbon dioxide are 960K, 1290K and 3384K. The 960K mode is degenerate with a degeneracy of two. Since the stagnation temperature of the flow is 710K the last mode can be neglected without any significant errors. The thermo-chemical processes modeled are translational-rotational relaxation and vibrational-translational relaxation. The vibrational relaxation rates are obtained from Boyd[12]. All vibrational modes are assumed to be in equilibrium with each other and to have the same relaxation rates. This assumption is made due to the lack of information about separate modes. The rotational relaxation rates are obtained from a previous study by Boyd[12]. The implementation of these relaxation effects is similar to the one described in previous chapter.

For solutions of the Navier Stokes equations, viscosity has to be prescribed as a function of the flow properties such as pressure or temperature. The viscosity model used has a temperature coefficient of 0.67 and gives an excellent fit to measured data.[12] This model has been used before for numerical studies of CO_2 flows using the DSMC method[12].

6.3.2 Boundary conditions

The simulation domain starts at the inlet to the nozzle and goes into the far-plume region. There are four types of boundaries, the inlet to the nozzle, the nozzle wall, the axis centerline and the outflow. Boundary conditions are implemented using fictitious cells outside the boundaries. At the inlet plane the flow is sub-sonic. For a CFD simulation, this allows us to specify two properties at the inflow boundary while a third has to be extrapolated from inside the domain. From the experimental measurements of the nozzle flow, mass-flow rate and stagnation temperature are known and hence they are specified at the nozzle inlet. The velocity is extrapolated from inside the domain. The axis centerline is implemented as a line of symmetry.

The outflow boundary condition depends on the Mach number of the flow normal to the domain exit plane. If the flow is supersonic all the flow properties are extrapolated from inside the flow domain. If the flow is subsonic the pressure at the exit is assumed to correspond to the background pressure of the flow and all other flow properties are extrapolated or calculated. Since the experiments conducted were of the flow expanding into vacuum, the backgound pressure is very low. For the simulations, the background pressure is set to a low value of 0.01 Pa. The actual value of the pressure does not affect the flow. The domain is made large enough so as to minimize the effects of the exit boundary conditions in the regions of interest.

The nozzle wall is simulated using an isothermal wall boundary condition. The CFD code requires the wall temperature as an input parameter. Since the stagnation temperature of the flow is 710K and the room temperature is 300K, it is reasonable to expect the wall temperature to be bounded by these values. The wall temperature may not be uniform and could vary from the nozzle throat to the nozzle lip. For the simulations described in this chapter, the wall temperature is assumed to be uniform. Two simulations are performed, one with a wall temperature at 300K and another with the wall temperature at 500K.

Calculating the boundary layer thickness provides a simple estimate of the effect of the wall temperature. The boundary layer thickness on a flat plate is inversely proportional to square root of the Reynolds' number and therefore to the square root of viscosity. This simple estimate predicts that the boundary layer for a wall temperature of 500K would be about 25% thicker than the boundary layer for a wall temperature of 300K. The CFD results can thus be expected to be sensitive to the wall temperature.

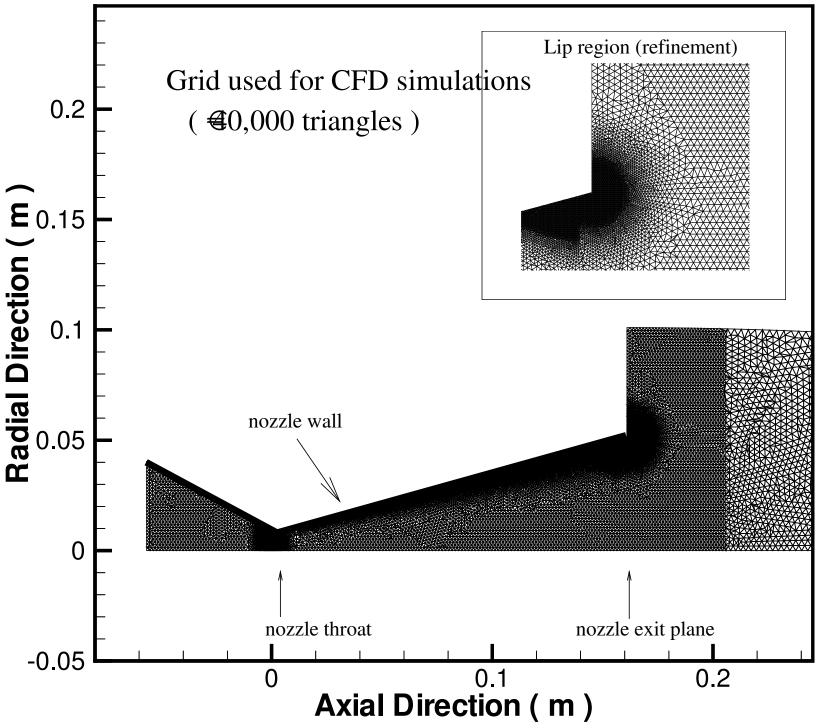

Figure 6.1. Grid used for the CFD computations

6.3.3 Grid resolution and other numerical issues

The domain starts at the inlet plane of the nozzle and extends about ten nozzle radii from the nozzle exit-plane in the axial direction and about one nozzle radius from the nozzle lip in the radial direction. The backflow region is not included as the flow is expected to be highly non-continuum in that region. Figure 6.1 shows a sample grid used for the simulations. The grid is clustered near the wall, the nozzle throat, and the nozzle lip to adequately capture the flow. A grid independent solution is obtained by repeating the simulations on finer grids until grid resolution is sufficient. The coarse grid has around 10,000 cells while the final grid has about 40,000 cells. Only results from the final grid are presented in this chapter.

6.4 Comparison of CFD Results with Experimental Measurements

This section presents the comparison of the results obtained from the CFD computations with experimental measurements.

6.4.1 Pitot pressure

Measurements of centerline pitot pressure as a function of axial distance were made using probes having diameters of 0.05”, 0.125” and 0.25”. The measurements indicated that the pitot pressure was independent of probe size. The details of the measurements are presented in Bailey’s report[9]. Pitot pressure is not directly predicted by the simulations. It can however be calculated using the pressure, temperature, and Mach number values predicted by the simulation along with normal shock relations and γ, the ratio of specific heats. This last quantity is calculated using information about the translational, rotational and vibrational temperatures.

Figure 6.2 shows the comparison between the values calculated using the CFD results and the measurements. The figure shows that the CFD results are sensitive to the wall temperature. However, the two CFD results bound the experimental results, thereby suggesting that a more accurate modeling of the wall boundary conditions might result in better agreement between experimental and numerical results. The 500K case shows better agreement with the experimental measurements and is used for all other comparisons presented in this chapter.

In the experimental report, the measured values of pitot pressure, stagnation temperature and stagnation pressure are used along with isentropic relations with

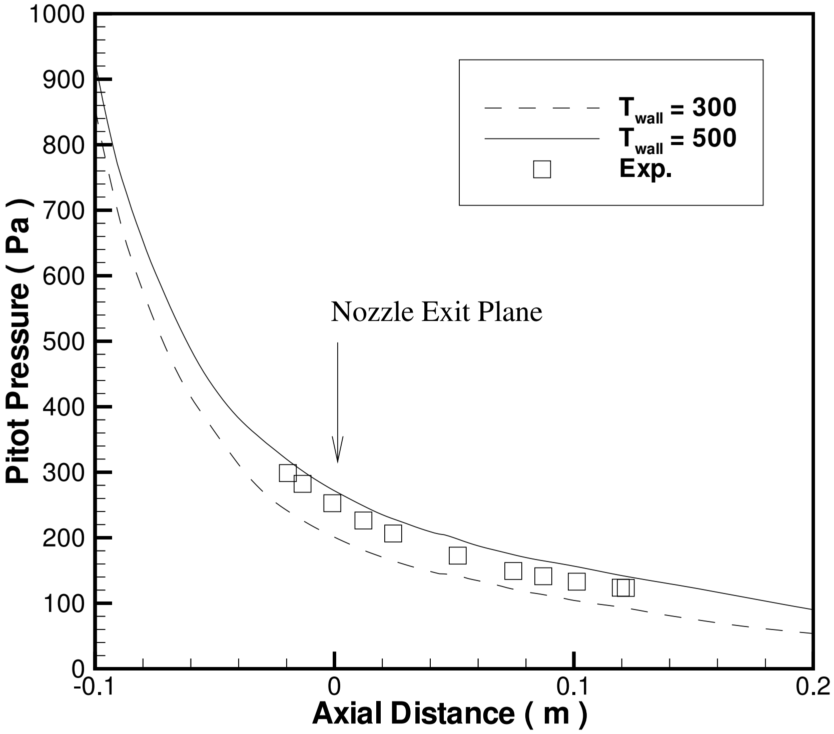

Figure 6.2. Comparison of centerline pitot pressure measurements with of data calculated from the simulations

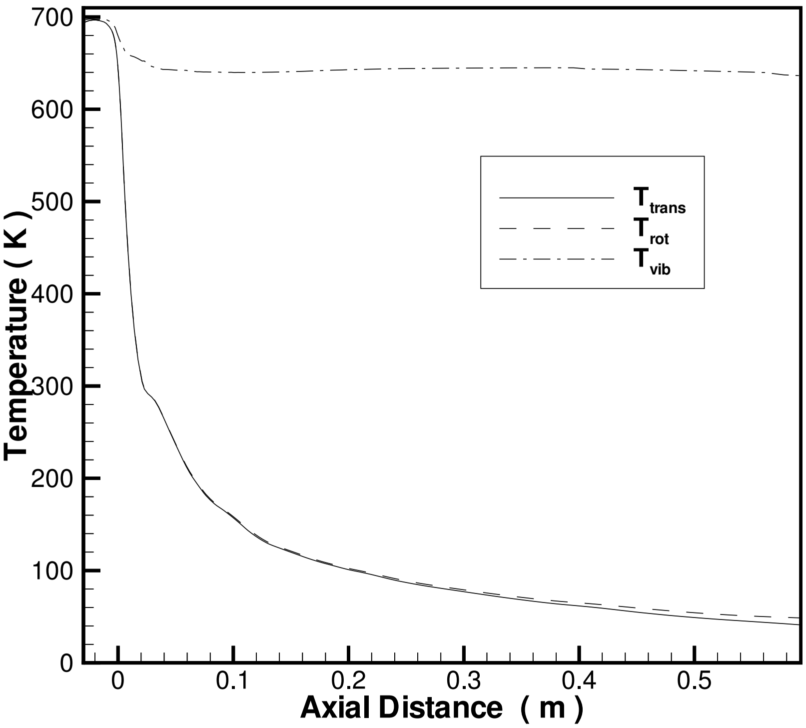

Figure 6.3. Centerline temperatures predicted by the simulation

the assumption that $\gamma = 1.4$ to derive the flow properties along the axis.[9] Since the CFD simulations include detailed thermo-chemical modeling, the accuracy of these assumptions can be assessed. Calculation of γ from the translational, rotational and vibrational temperature data shows that it is close to 1.2 instead of 1.4 assumed for data reduction. Figure 6.3 shows profiles of different temperatures along the axis centerline. The rotational and the translational modes are in equilibrium throughout while the vibrational temperatures are almost frozen after the nozzle throat. It should be noted that the vibrational temperature in these non-equilibrium flows is simply an index of the energy contained in the vibrational mode. Also the different modes of vibrational energy are not modeled separately, thereby giving a single vibrational temperature. These finite rate processes are irreversible and increase the entropy of the flow thereby violating the isentropic assumption.

6.4.2 Flow angle

Flow angle was obtained by measuring the variation of the pitot pressure with probe angle to the incident flow. The angle at which the maximum of pitot pressure occurred was assumed to be the angle of the flow velocity vector at that position in the nozzle plume.

One of the important conclusions of the experimental report is the re-affirmation of some observations made by Bird[13] based on DSMC computations. Bird had seen that in the boundary layer flow upstream of the nozzle lip, the local flow angle is greater than the local angle of the nozzle wall i. e. the flow is directed towards the nozzle wall rather than parallel to it. The experiments indicated that flow angles of up to 30 degrees are possible in the exit plane, indicating local flow

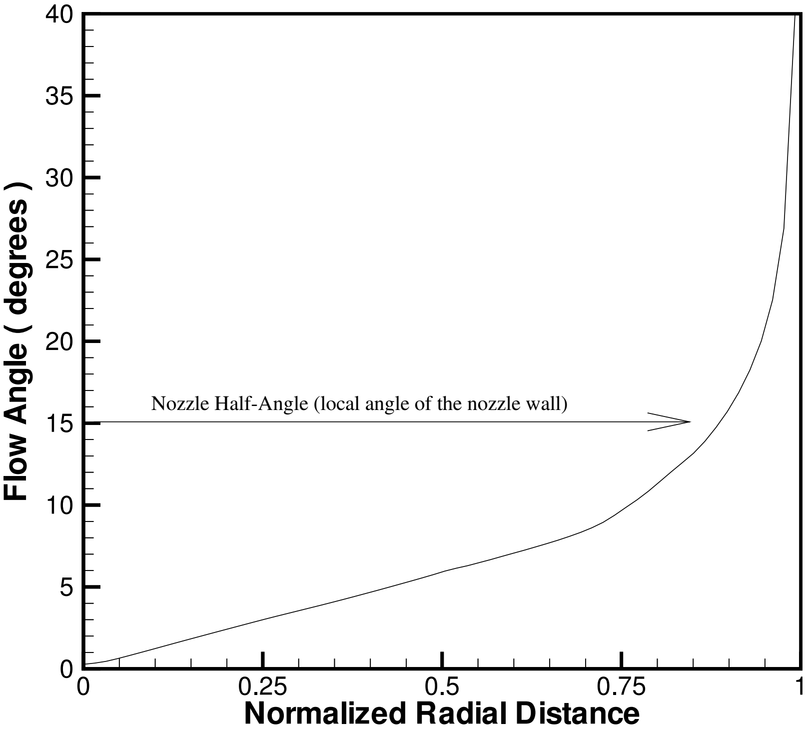

Figure 6.4. Flow angle across the nozzle exit plane

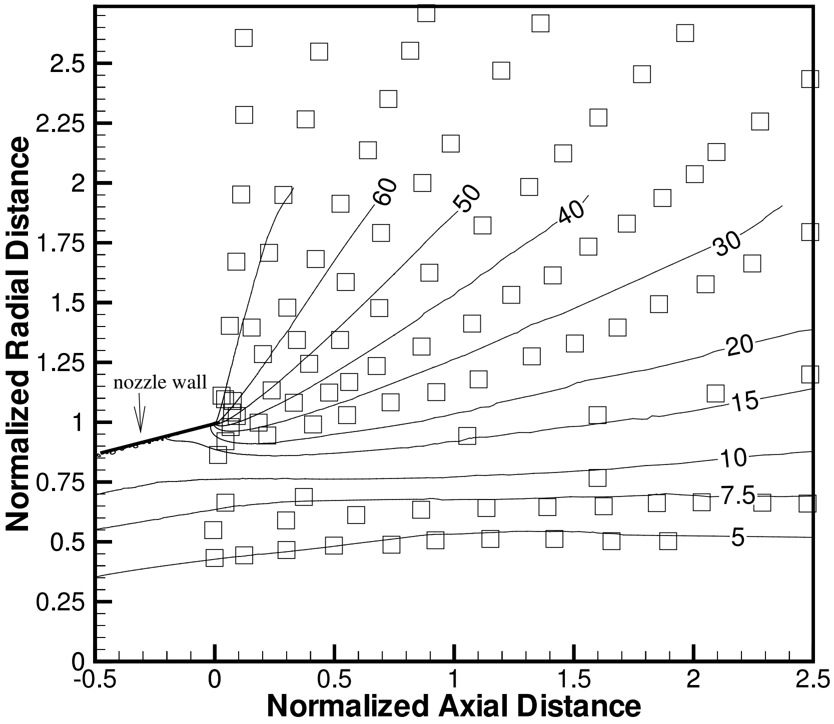

Figure 6.5. Comparison of contours of flow angles

angles with respect to the wall of 15 degrees, which is of the magnitude observed in Bird's studies. Figure 6.4 shows the flow angles predicted by the simulations at the nozzle exit plane. The flow angles near the wall are close to 40 degrees. This provides additional numerical evidence of this phenomenon. Thus, the Navier-Stokes code used for this study is able to overcome the limitations of the boundary layer codes mentioned in the experimental study which do not account for this effect.

The flow angle data from the experimental measurements were presented as contours of constant flow angle. To accomplish this, best-fit lines (by eye) were drawn through the experimental data. To make comparisons with numerical data,

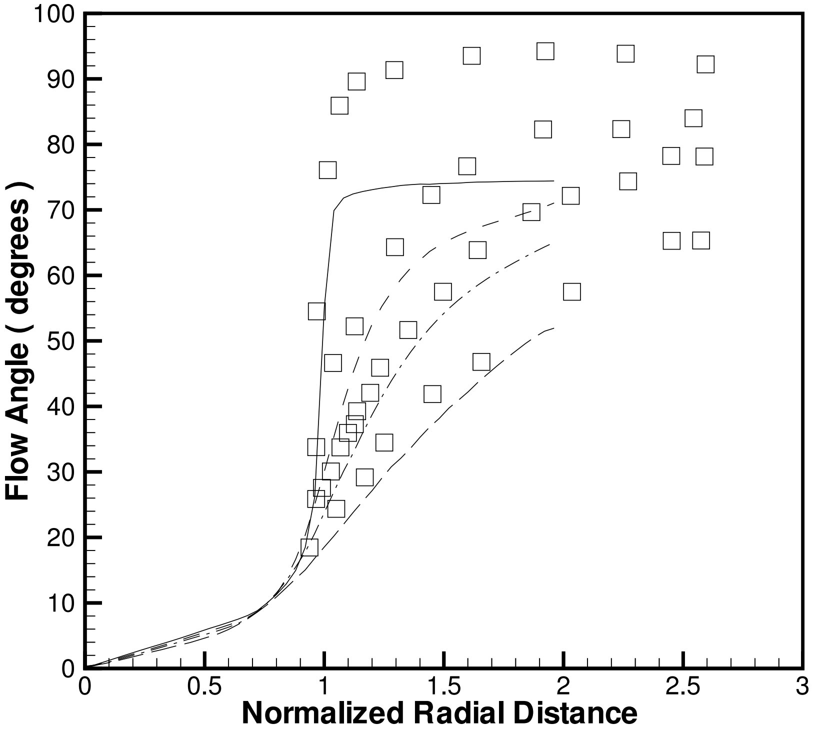

Figure 6.6. Comparison of radial profiles of flow angles

the contour plots presented in Bailey's report were digitized and plotted along with flow angle contours obtained from the simulations. Figure 6.5 shows a comparison between the flow angle measurements and numerical predictions. The location and frequency of the symbols is an artifact of the digitization and do not have any relevance to the experimental measurements. Taking into account the numerous inaccuracies introduced, it can be concluded that the overall agreement is reasonable. In the central-core region of the flow there is excellent agreement between the measured values and the numerical predictions. As we go away from the nozzle centerline, the CFD flow seems to show a larger deflection from the centerline than that inferred from the experimental measurements.

Figure 6.6 presents a comparison of flow angle profiles along the radial direction at four axial stations. The agreement deteriorates as we go away from the axis. Bailey's report suggests that flow angle measurements in regions of high shear might be susceptible to probe flow interaction effects. Near the nozzle lip, the probe bow shock may interact with the nozzle lip and lead to inaccuracies in the measurements. As we go away from the centerline the plume flow becomes highly rarefied and non-equilibrium effects become important. Under these conditions, the underlying assumptions of the CFD code may not be valid leading to poor results.

6.4.3 Number density and Temperature

Number density measurements, obtained using the electron beam fluorescence technique, were derived from measurements of the light intensity within a given spectral interval of a vibrational-rotational band of a molecular species generated as a result of the interaction of a narrow collimated beam of electrons with the gas species.

Figure 6.7 shows comparisons between axial profiles of number density. In order to obtain accurate measurements of absolute number density using this technique, it is necessary to calibrate the system in a gas of known number density. For the experimental program, estimates of number density on the nozzle centerline were derived from the measured value of pitot pressure, stagnation pressure, the assumption of isentropic flow and a γ of 1.4. The electron beam calibration factor was selected on the basis of this calculated value of number density close to the nozzle exit plane. This calibration method might have introduced additional errors. Also the computed results are sensitive to the wall boundary conditions. Keeping these two factors in mind, the overall agreement between the computed

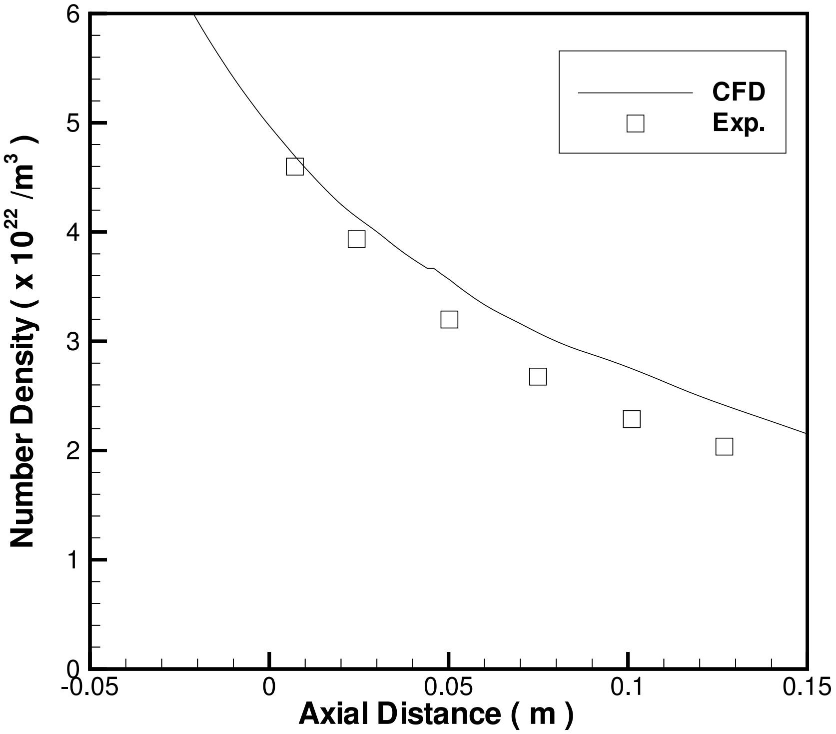

Figure 6.7. Centerline number density from numerical calculations and experiments

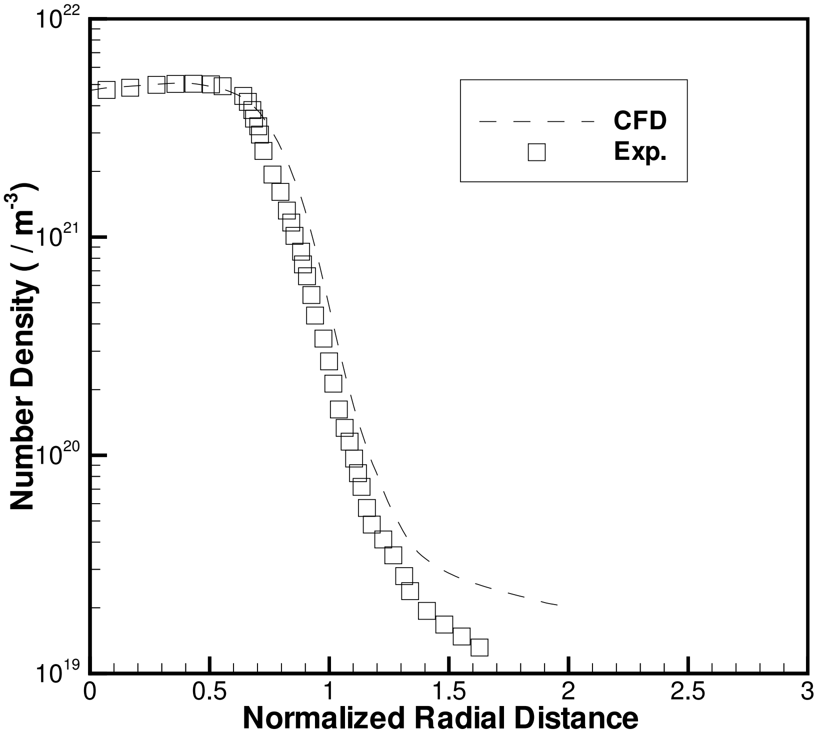

Figure 6.8. Number density profiles along the radial direction at a distance of 0.27" from the nozzle exit plane

and measured values is satisfactory.

Figure 6.8 shows comparison between radial profiles of number density an axial station 0.27" from the nozzle exit plane. The values reported by Bailey[9] are digitized and plotted. The locations of the symbols are an artifact of the digitization and do not have any significance to the experiments. There is good agreement between CFD results and experimental measurements in the core-flow region though the CFD results are slightly higher. The agreement between the measured and computed values deteriorates after a distance of about 1.3 nozzle radii from the centerline. After that, the CFD number density drops at a much slower rate while the experimental measurements show a continued rapid decrease in number den-

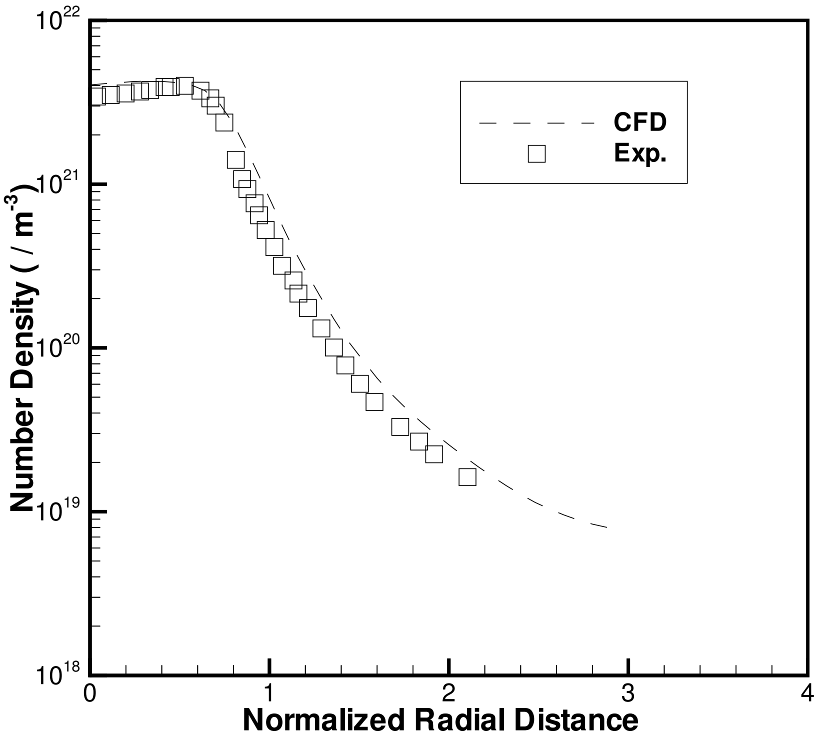

Figure 6.9. Number density profiles along the radial direction at a distance of 1.27” from the nozzle exit plane

sity. The CFD results may not be accurate in these regions because of the very low number densities involved. The DSMC results and the breakdown parameter calculations presented in the later sections support this conclusion.

Figure 6.9 shows comparison between radial profiles of number density at a second axial station, 1.27” from the nozzle exit plane. Here the agreement is good throughout the region of comparison. The experimental profiles show an off axis peak in the number density. The maximum number density occurs at the edge of the high-density core region rather than on the centerline. Bailey[9] concluded that this was not an artifact of the measurement technique based on experimental data obtained from previous studies. These off-axis peaks can be observed in the

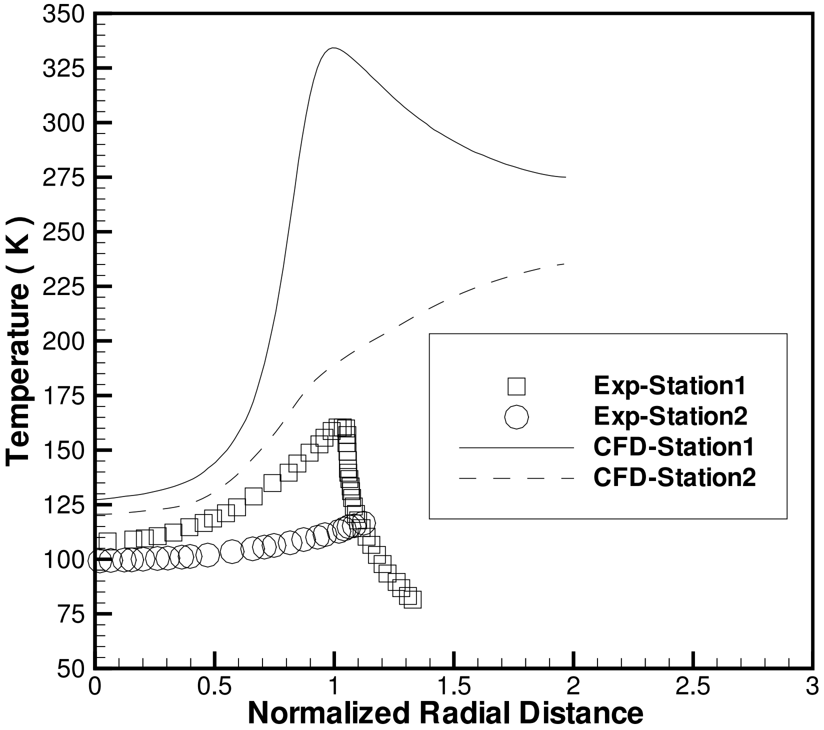

Figure 6.10. Rotational temperature profiles along the radial direction at the two axial stations

simulation results also, thereby confirming the assumption that they are indicative of changes in the flow field properties in the core-flow region. These off-axis peaks are not as prominent in the simulation results as they are in the experimental measurements.

Rotational temperature was determined by the measurement of the spectral line intensity distribution within a vibrational-rotational band of a molecular species generated as a result of the interaction of a narrow collimated beam of electrons with the gas species. These measurements used isentropic prediction of the exit-plane rotational temperature for calibration, which may have affected the accuracy of these measurements. The nozzle centerline value of 108K seen in the experimental results is the same as the isentropic prediction for temperature at this station with a γ of 1.4.Figure 6.10 shows the rotational temperature comparisons at the two axial stations. The CFD predictions of the temperatures are much higher than the experimental measurements. The experimental measurements and the CFD results show similar behavior although the experimental data show a much steeper drop in the expansion region. The CFD results predict a peak temperature of about 325K while the experiments show a peak of about 160K.

6.5 Conclusions

This chapter presents the comparison between CFD results and experimental measurements obtained at the AEDC. The computational results were found to be sensitive to the wall temperature. Experimental measurements of pitot pressure along the centerline were compared with calculations based on the CFD simulations. The computed values were close enough to experimental measurements to suggest that the physics of the flow was captured accurately. A more detailed modeling of the wall boundary condition might give better numerical agreement with the measured results.

Detailed relaxation modeling of the different energy modes of CO_2 indicated that the vibrational mode was frozen in the diverging portion of the nozzle and in the plume. The CFD simulations also predicted regions of rotational nonequilibrium inside the plume. The central core region of the flow was non-isentropic and had a ratio of specific heats close to 1.2. This invalidates the isentropic flow assumption and the value of 1.4 used for calibrating some of the experimental measurements.

The computations re-confirmed earlier findings about the behavior of the flow near the nozzle lip. Flow angle measurements were compared with the computed values and found to agree in the central-core region of the flow. The CFD predictions of radial profiles of number density showed good agreement within regions of validity of the continuum approach.

This completes the presentation of the results for the nozzle and near plume region. Results in the plume and an analysis of breakdown of continuum will be presented in the next chapter.

Chapter 7

Breakdown of continuum

After validating the CFD code and performing the nozzle flow simulations, the next step in the development of the combined methodology is the investigation of breakdown of the continuum approach. This chapter presents parameters that can be used to predict breakdown of continuum. The results from CFD computations are compared with results from DSMC computations. The numerical results are then compared with experimental results to assess the validity of the continuum assumption. The DSMC simulations are analyzed in detail to explain the failure of the continuum approach

7.1 Introduction

The CFD method has physical and numerical limitations that prevent it from being used for very rarefied flows. Since the outer plume and back-flow regions involve very low densities, the DSMC method is used for performing simulations in these regions. For the most efficient utilization of the two methods, a method for accurately determining the validity of the continuum approach is required. In the combined methodology, the CFD results are analyzed and a parameter based on the flow properties is calculated and used to assess the validity of the CFD simulation.

This chapter looks at a few possible parameters. A new parameter is presented which is used to split the domain into a CFD region and a DSMC region. DSMC simulations are then performed. The DSMC simulations are initialized with the results from CFD simulation. The results obtained from the DSMC simulations are compared with the CFD results. The numerical results are also compared with experimental measurements.

One of the objectives of this study is to investigate a flow regime where the CFD approach breaks down and the DSMC approach gives accurate results. Comparisons with experimental measurements are performed with the objective of finding a region where the experimental measurements agree with the DSMC results and disagree with the CFD results. The DSMC results in this region are then analyzed in detail to understand why the CFD method fails to make accurate prediction of the flow properties.

7.2 Prediction of breakdown

The breakdown of the Navier-Stokes equations under conditions of low-density, hypersonic flow has been investigated before by Boyd et al[14] and for expanding flows by Bird[13]. Both papers present parameters which can be used for prediction of breakdown of the continuum approach.

7.2.1 Parameters used in previous studies

The gradients of the macroscopic flow properties in an isentropic flow depend only on the size of the flow. However, these changes in the macroscopic flow properties can occur only through intermolecular collisions and, as the density falls, the collision rate becomes too low for the maintenance of these gradients. Bird studied the occurrence of this type of breakdown in gaseous expansions and found that the breakdown correlates with a parameter

$$P = -\frac{1}{\nu}(\frac{D(\ln \rho)}{Dt}), \tag{7.1}$$

where ν is the collision frequency and ρ is the density. $\frac{D}{Dt}$ refers to the substantial derivative. For a steady flow, this equation can be written as

$$P = -\frac{\pi^{\frac{1}{2}}}{2} s \frac{\lambda}{\rho}(\frac{d\rho}{dx}). \tag{7.2}$$

Here s is the speed ration, λ the local mean free path and the gradient is evaluated in the stream-wise direction. The initial breakdown in both steady and unsteady expansions was found to correlate with a value of P of approximately 0.04, thereby giving an empirical criterion for breakdown.

The evaluation of the gradient in the stream-wise direction introduces the velocity components into the evaluation of the breakdown parameter leading to possible problems at stagnation points and low velocity flows. Boyd studied a variety of breakdown parameters and concluded that a Knudsen number based on the local density-gradient length scale is best suited for most applications. Studies indicate that the continuum approach fails when this breakdown parameter approaches 0.05.[14]

There are two problems with using these parameters for a combined CFD-DSMC approach. The cut-off value of these parameters is empirical and might vary with geometry and flow conditions. These parameters are based on density gradients and do not consider gradients of other macroscopic properties. When using a combined approach, a parameter that shows a clear distinction between regions where the CFD solution is valid and regions where it is not valid would be ideal. Since the breakdown of the CFD approach is related to viscosity and heat transfer, it should take both these transport phenomena into account.

7.2.2 Chapman-Enskog Approach

It is possible to approach the prediction of breakdown from a kinetic theory viewpoint. The Navier-Stokes equations can be derived from the Chapman-Enskog solution to the Boltzmann equation. The Chapman-Enskog solution results from an expansion of the velocity distribution function for small departures from the Maxwellian distribution function present at equilibrium. The Chapman-Enskog distribution function can be written as

$$f(\vec{C}) = f_0(\vec{C})\Gamma(\vec{C}), \tag{7.3}$$

where $f_0(\vec{C})$ is the Maxwell-Boltzmann velocity distribution function, where $\vec{C} = \mathbf{C}/\sqrt{2kT/m}$ is the velocity normalized with the thermal velocity, k is the Boltzmann constant, T is the temperature and m is the particle's mass.

$$\begin{aligned}\Gamma(\vec{C}) = 1 + (q_x C_x + q_y C_y + q_z C_z)(\tfrac{2}{5}C^2 - 1)\\ -2(\tau_{x,y} C_x C_y + \tau_{x,z} C_x C_z + \tau_{y,x} C_y C_z)\\ -\tau_{x,x}(C_x^2 - C_z^2) - \tau_{y,y}(C_y^2 - C_z^2)\end{aligned} \tag{7.4}$$

and

$$q_i = -\frac{\kappa}{p}(\frac{2m}{kt})^{1/2}\frac{\partial T}{\partial x_i} \tag{7.5}$$

$$\tau_{i,j} = -\frac{\mu}{p}(\frac{\partial v_i}{\partial x_j} + \frac{\partial v_j}{\partial x_i} - \frac{2}{3}\frac{\partial v_k}{\partial x_k}\delta_{i,j}) \tag{7.6}$$

where $\tau_{i,j}$ and q_i are the dimensionless heat flux and the stress tensor[16]. The viscosity and thermal conductivity are μ and κ, respectively. v_k is the fluid velocity and T is the temperature. C_x, C_y and C_z are the components of $\vec{C}$ and C is the speed.

This derivation assumes the perturbation to the Maxwellian to be small compared to 1. Thus the magnitude of this perturbation gives an indication of the validity of the Navier-Stokes equations. This approach takes into account both transport phenomena. Momentum transfer is accounted for through the shear stress terms in the expression and heat transfer through the thermal stress terms. This expression is evaluated using the mean velocity, the shear stress and heat fluxes obtained from a Navier-Stokes simulation and can be used to assess the validity of the simulation.

The other advantage of using this parameter is evident when we examine the radial profiles of the breakdown parameter. Figure 7.1 shows the breakdown parameters plotted along the radial direction at an axial station 0.27" from the nozzle exit. The Chapman-Enskog factor gives a clear limit for the size of the CFD domain. It can be seen that after about 0.9 nozzle radii this factor falls rapidly. This can be also verified in Fig. 7.2 which shows the three parameters plotted at another axial station, 1.27" from the nozzle exit. In this case, as expected breakdown is predicted at a greater distance from the axis. The comparisons between CFD results and experimental measurements of number densities at these stations are presented in the earlier section, Figs. 6.8 and 6.9. The CFD results agree with experimental measurements for about .25 times the nozzle radius. Thus this parameter does not exactly predict where the CFD results are not accurate but gives us a good indication of the appropriateness of using the CFD code without any

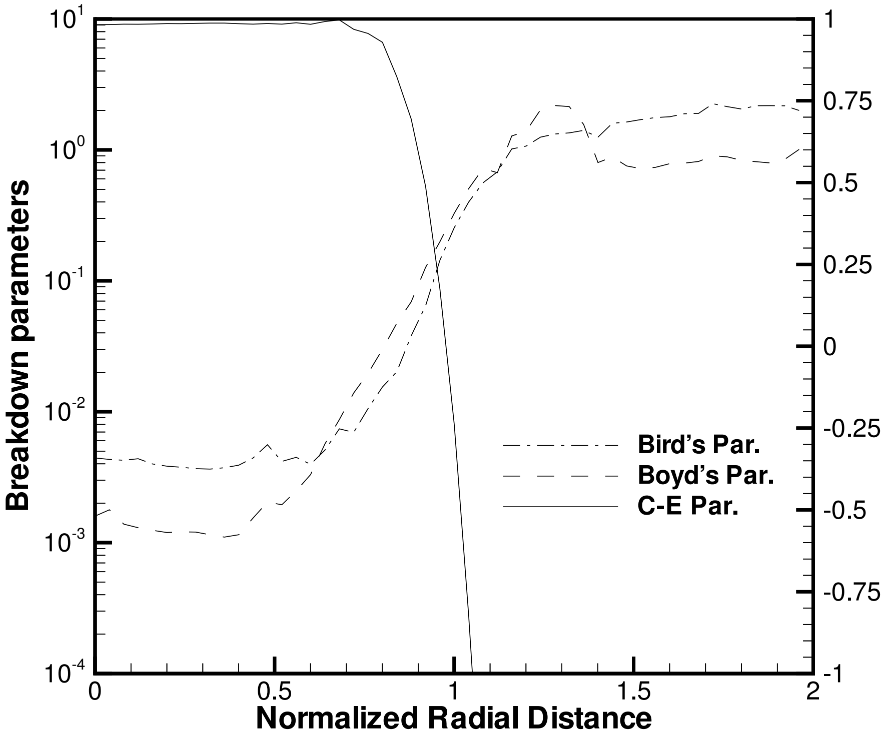

Figure 7.1. Comparison of breakdown parameters along the radial direction at a distance of 0.27" from the nozzle exit plane

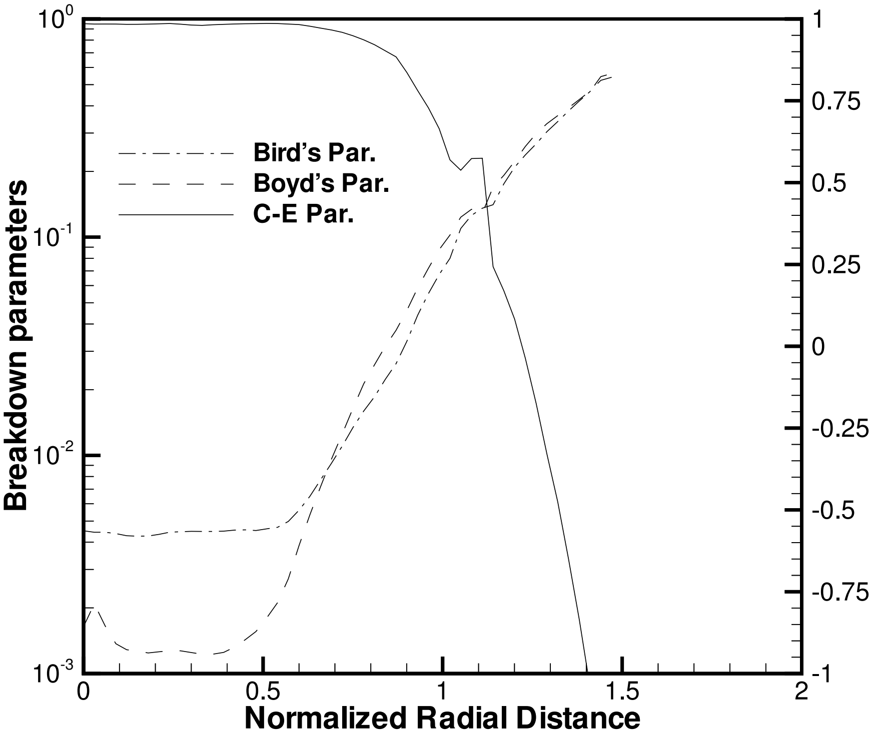

Figure 7.2. Comparison of breakdown parameters along the radial direction at a distance of 1.27" from the nozzle exit plane

reference to any empirical factors. Since the breakdown criterion is not totally empirical, this method could be applied to the study of other flows also.

7.3 DSMC simulations of the outer-plume region

The DSMC code used is described in chapter four. For this study the code is used with unstructured triangular grids. A sub-cell method[18] is used to reduce the computational cost. The results from the CFD simulations are used as inflow boundary conditions for the DSMC code. Maxwellian distributions of velocities are assumed at the inflow. Since the CFD simulations showed very little change in the vibrational temperature in the plume, the vibrational mode is assumed to be frozen and is not included in the DSMC simulations. Thus the gas is assumed to have 3 translational modes and 2 rotational modes of freedom. The implementation of rotational relaxation is based on an earlier work by Boyd et al.[12].

The simulations are performed on an IBM SP2. There are about 1.2 million particles in the simulation. The grid used has about 10,000 cells resolved to the level of about 5 times the mean free path. Sub-cells are of uniform size and resolved to the level of the smallest mean free path. Care was taken to ensure that at least a few particles per sub-cell are present. Figure 7.3 shows the grid used for the DSMC simulations.

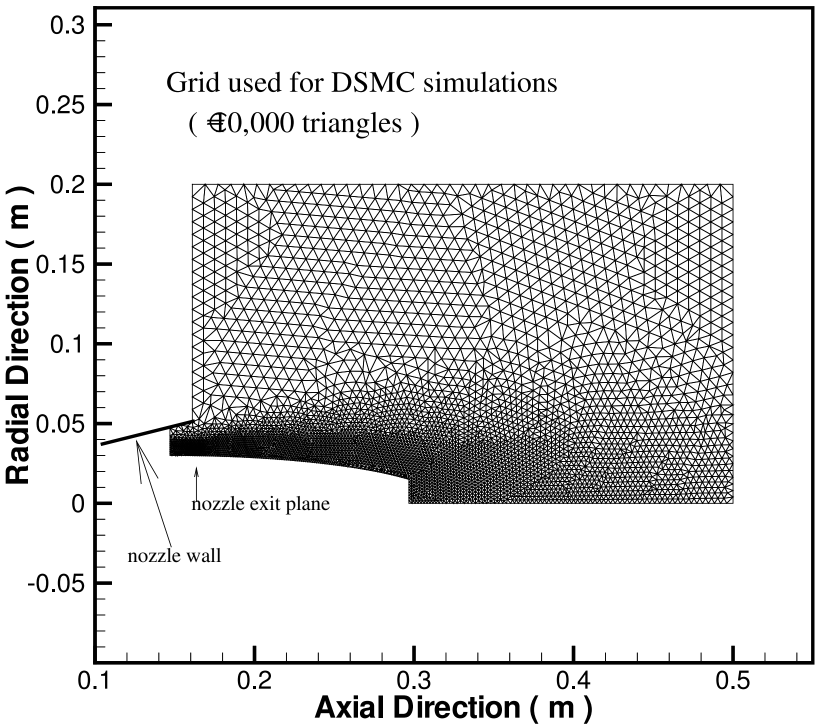

Figure 7.3. Grid used for the DSMC computations

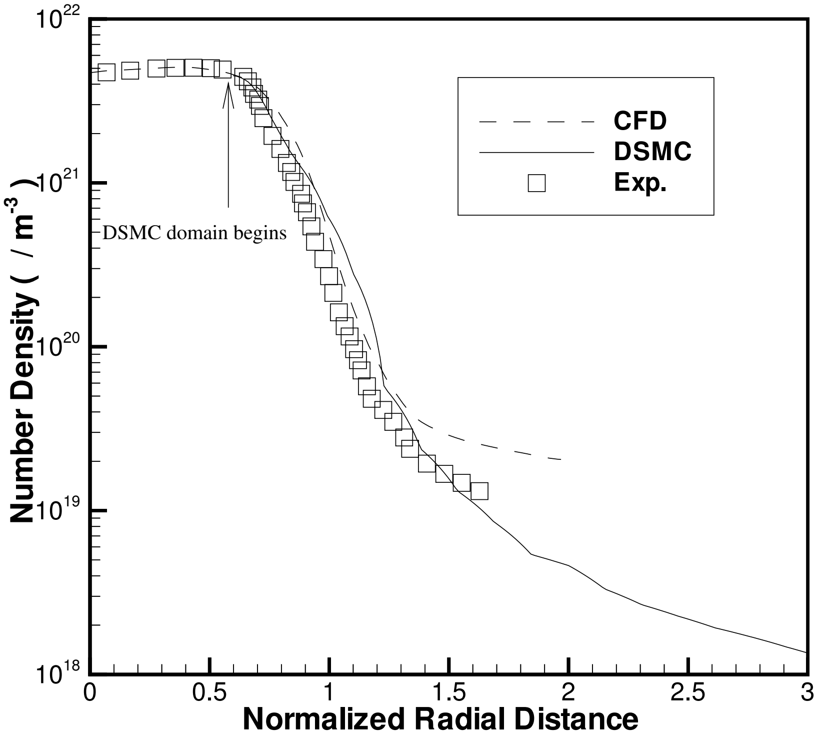

Figure 7.4. Number density profiles along the radial direction at a distance of 0.27" from the nozzle exit plane

7.4 Comparison of the DSMC results with CFD results and experiments

The results obtained from the DSMC simulation are compared with results obtained from the CFD computations. To assess the accuracy of these numerical results, they are compared with experimental measurements. Figure 7.4 shows the number density profiles at 0.27" from the nozzle exit plane along the radial direction. The solid line and the dotted line represent the values obtained from DSMC and CFD simulations respectively. The symbols represent values obtained from experimental measurements. The DSMC domain begins about half a nozzle radius from the axis centerline. Up to about 1.2 times the nozzle radius there is good agreement between all three values. The CFD results then diverge away from the other two results. There is good agreement between DSMC predictions and experimental measurements of number density throughout the region of measurement. Since both the CFD and the DSMC methods use similar kinetics models, the agreement between DSMC results and experimental measurements seems to indicate that the continuum approach is not valid in these regions. This is further supported by the calculated breakdown parameter values shown in Fig. 7.1. It can be seen that all three breakdown parameters predict breakdown of the Navier-Stokes equations before the CFD number density starts differing from the other two.

Figure 7.5 shows a similar plot with the number density profiles at 1.27" from the nozzle exit plane along the radial direction. There is very good agreement between numerical results and experimental measurements of number density throughout the region of measurement. The behavior shown by the CFD results

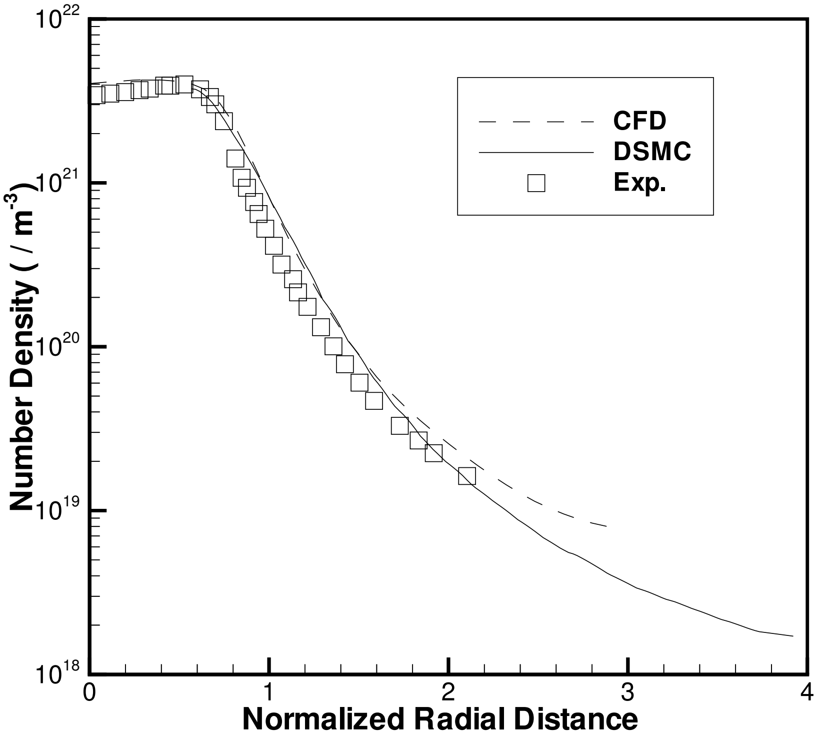

[c]

Figure 7.5. Number density profiles along the radial direction at a distance of 1.27" from the nozzle exit plane

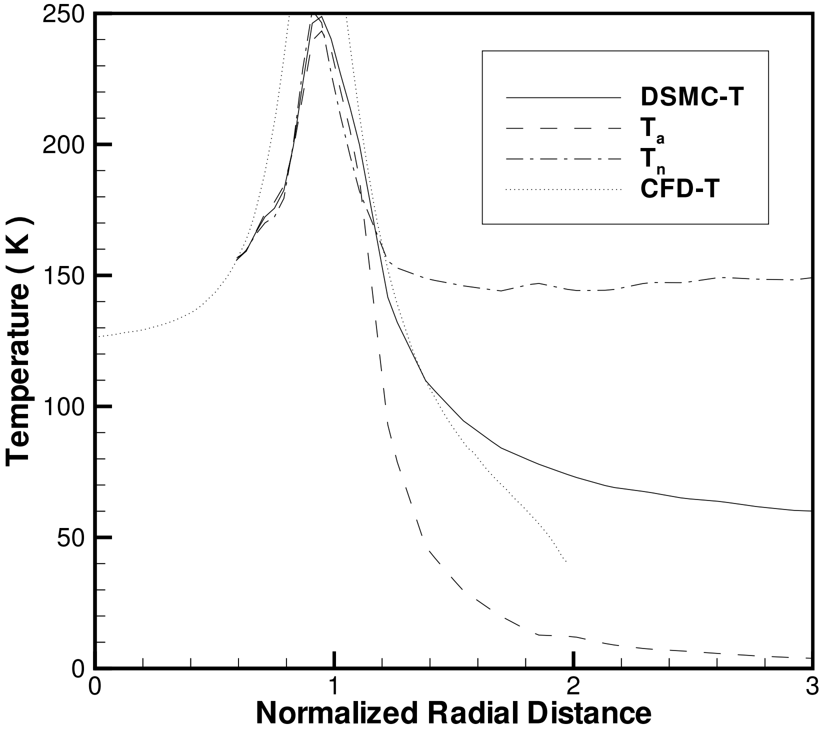

Figure 7.6. Translational temperature profiles along the radial direction at at distance of 0.27” from the nozzle exit plane

in the previous station may be starting to appear at the edge of the CFD domain.

7.5 Analysis of breakdown

This section presents the analysis of DSMC results for a better understanding of the breakdown of Navier-Stokes equations. Figure 7.6 shows radial profiles of temperatures at 0.27” from the nozzle exit plane. The solid line is the DSMC prediction of translational temperature. The two dashed lines show component-wise temperature profiles. The axial temperature falls rapidly from its peak close to the nozzle lip and reaches a very small value about 2 nozzle radii from the axis centerline.

The normal temperature freezes at 150K at a distance of 1.15 nozzle radii from the axis centerline. The number densities in these regions are very low and there are not enough collisions to maintain the drop in temperature predicted from geometric considerations. The Navier-Stokes equations are based on the assumption of translational equilibrium and involve a single translational temperature. The dotted line shows the translational temperature predicted by the CFD simulations. Since the rate of decrease of temperature is imposed on the CFD solution from geometric considerations, the CFD translational temperature continues to drop. As the normal temperature freezes, the DSMC translational temperature flattens out. So after about 1.2 nozzle radii from the centerline the CFD predictions of temperature fall below the DSMC predictions. Since pressure is determined mainly from momentum considerations, the continued drop in temperature is compensated by a flattening number density profile. Thus the CFD predictions of number density are higher than the experimentally measured values and the DSMC predictions.

Figure 7.7 shows the number density results presented earlier superimposed on a plot of the ratio of normal to axial temperature. This ratio can be considered as an index of translational non-equilibrium. At about 1.2 nozzle radii from the axis centerline this ratio falls rapidly indicating the onset of freezing. It can be seen that in regions where freezing has occurred, the CFD results are not accurate.

Figure 7.8 shows the rotational temperature profiles at 0.27” from the nozzle exit plane along the radial direction. The solid line and the dotted line represent the values obtained from DSMC and CFD simulations respectively. The symbols represent values obtained from experimental measurements. There is reasonable agreement between the CFD and DSMC results while the experimental measurements are much lower. Figure 7.9 shows a similar plot with the temperature profiles

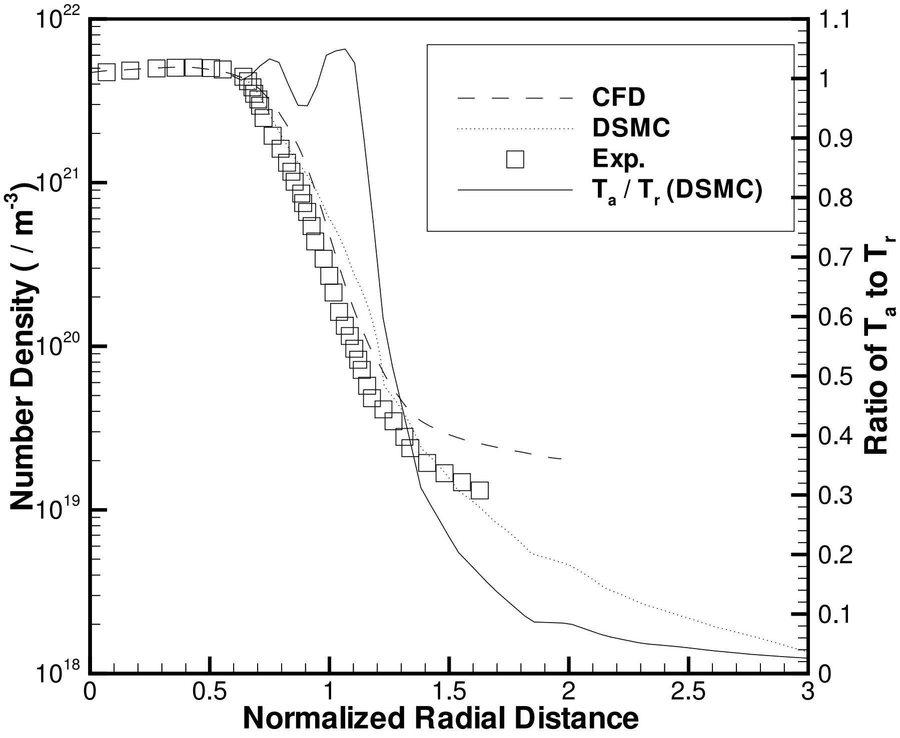

Figure 7.7. Number density profiles along the radial direction at a distance of 0.27" from the nozzle exit plane with an index of translational-equilibrium

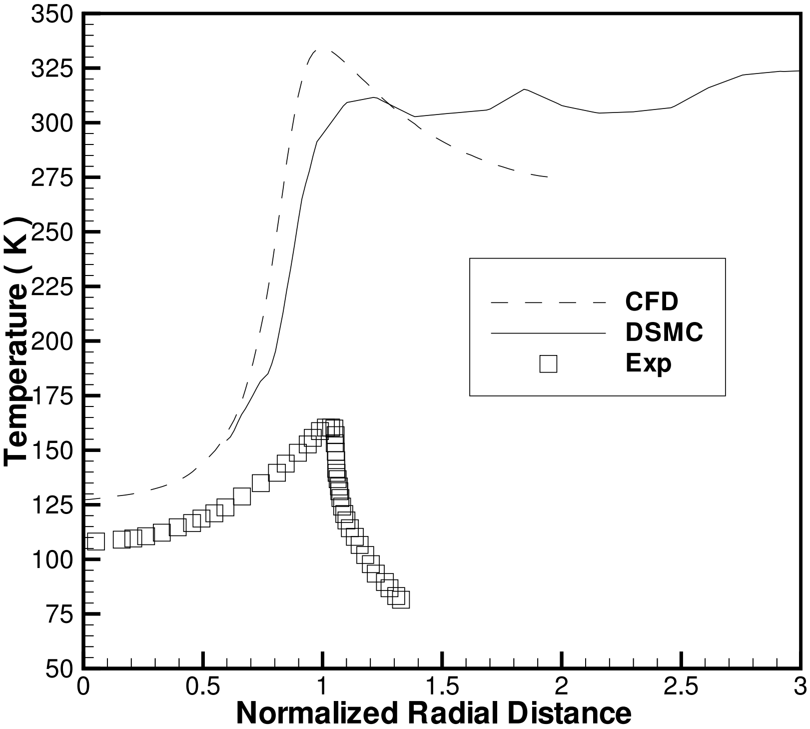

Figure 7.8. Temperature profiles along the radial direction at a distance of 0.27” from the nozzle exit plane

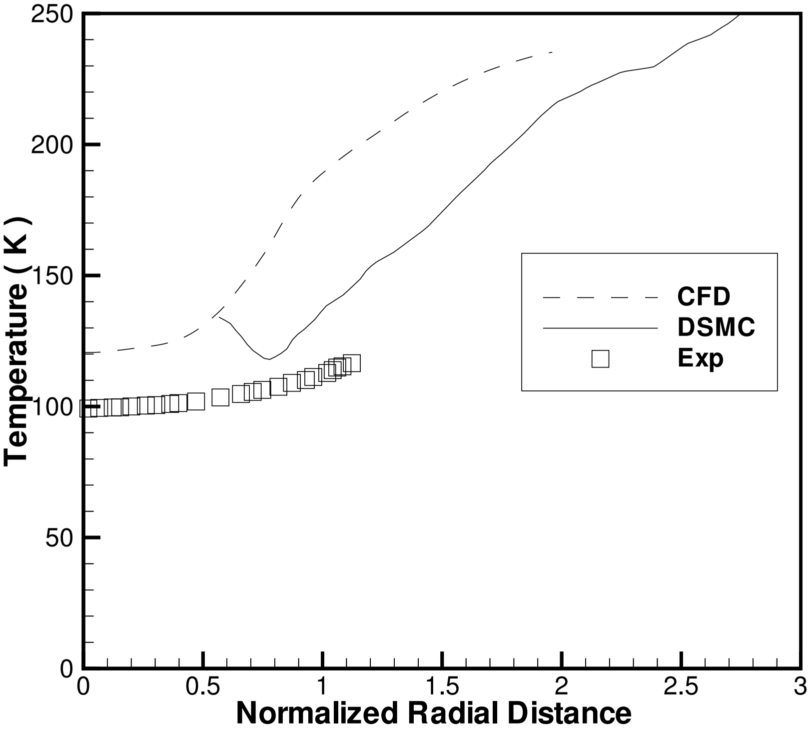

Figure 7.9. Temperature profiles along the radial direction at a distance of 1.27" from the nozzle exit plane

at 1.27” from the nozzle exit plane along the radial direction. The DSMC results and the CFD results show some difference. As shown in the previous section these regions involve flow regimes with translational non-equilibrium effects, which are not considered by the Navier-Stokes solver. The interface between the CFD region and the DSMC region is located where the temperature starts to increase. When the DSMC code is initialized this gradient information is not passed on to it and is therefore lost. These factors may account for the discrepancy between the two numerical results.

7.6 Conclusions

A breakdown parameter that can be used to split the computational domain into two regions, one to be solved using CFD methods and the other to be solved using DSMC methods, was presented. This parameter was used to split the domain by predicting the breakdown of the Navier-Stokes equations. DSMC simulations, of regions where CFD methods are not accurate, were performed. The DSMC predictions of radial number density profiles were then compared with the experimental measurements and found to be in good agreement, even in regions where the CFD results disagree with experiments. DSMC results were analyzed in detail in an attempt to investigate the failure of the CFD approach. It was found that the regions where CFD results are inaccurate corresponded with regions of translational non-equilibrium. Since the Navier-Stokes equations are based on the assumption of translational equilibrium, solutions to Navier-Stokes equations give inaccurate results for such flow regimes.

Thus a methodology for performing simulations of a complete nozzle-plume system was described. It involves a CFD simulation of the nozzle and near plume region, a breakdown parameter for splitting the domain, and a DSMC simulation of the outer plume regions where CFD is not valid. This approach is successfully applied to the study of CO_2 expansion into hard vacuum. The next step is to extend the simulation domain and perform simulations of the back flow region.

Chapter 8

Computation of back flow

This chapter describes the computation of the backflow region of the same carbon dioxide flow considered in chapter seven. The back flow region has very low number densities and is most accurately modeled using a DSMC computation. The DSMC computation is initialized using results from a CFD computation of the nozzle flow.

8.1 Introduction

Chemical rockets are used extensively for attitude control and other low thrust operations on trans-atmospheric vehicles and spacecraft. The interaction of the plumes from these rockets with the vehicle surface is a major source of concern for these applications. Plume impingement on the vehicle surface might lead to contamination of sensitive surfaces, thrust losses, disturbance torques and thermal loading. An accurate assessment of these issues requires detailed understanding of the fluid flow in the back-flow region.

This chapter presents the results of investigations on different methods for performing back-flow simulations. The computational results are compared with experimental measurements. Bailey's[9] study presents experimental measurements made in the back-flow region of the nozzle. The objective of our study is to investigate different methods for performing back-flow simulations and assess them using these experimental measurements.

Two experimental measurements are performed in the backflow region. Carbon dioxide number density measurements were accomplished using the electron beam fluorescence technique. Mass flux measurements were made in the back-flow region using a Quartz crystal microbalance. The computational results are compared with these experimental results.

First, a CFD computation of the nozzle and near plume region is performed. The Chapman-Enskog parameter described in the previous chapter is then used to predict breakdown. The DSMC domain starts where the Chapman-Enskog parameter has a value of 0.95. The grid used is show in figure 8.1. Bailey's report mentions that the results are sensitive to lip geometry. Care has therefore been taken to model the lip region in detail. The grid used has about 10,000 cells resolved to the level of about 5 times the mean free path.

A description of the DSMC code is presented in chapter four. A sub-cell method[18] is used to reduce the computational cost. The simulations are performed on an IBM SP2. There are approximately 1.2 million particles in the simulation. Sub-cells are of uniform size and resolved to the level of the smallest mean free path. Care is taken to ensure that at least a few particles per sub-cell are present.

The results from the CFD simulations are used as inflow boundary conditions for the DSMC code. Two methods of passing the information from the CFD simulations to the DSMC simulations are investigated. Since the CFD simulations show very little change in the vibrational temperature in the plume, the vibrational mode is assumed to be frozen and are not included in the DSMC simulations. Thus the gas is assumed to have 3 translational modes and 2 rotational modes of freedom.

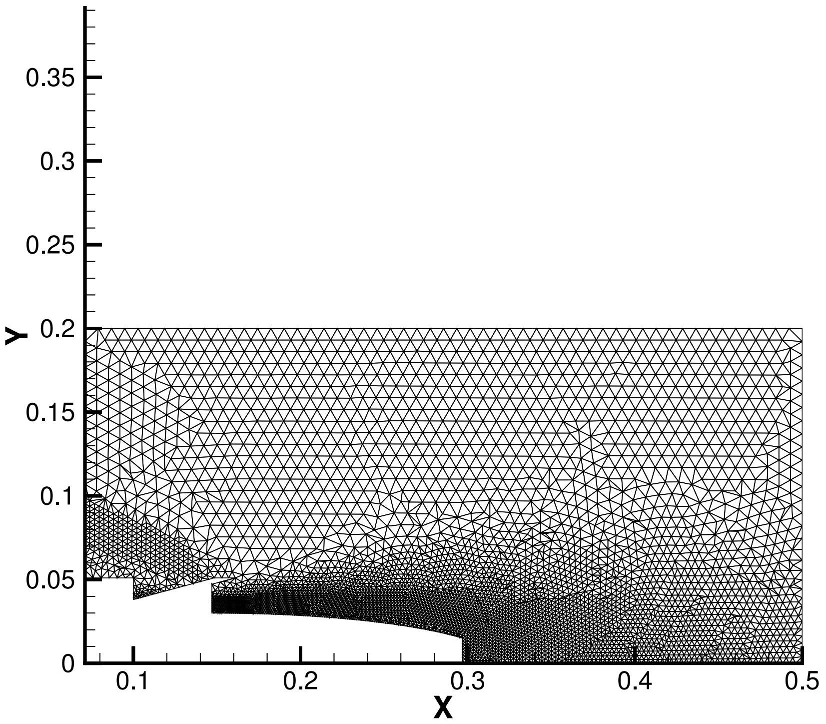

Figure 8.1. Grid used for the DSMC simulations

The implementation of rotational relaxation is based on an earlier work by Boyd et al.[12].

8.2 DSMC computation with Maxwellian boundary condition

The results from the CFD simulations are used as inflow boundary conditions for the DSMC code. The fluid properties need to be specified at the inlet of the domain. The temperature, velocity and number density are obtained from the CFD simulation and imposed as inflow boundary conditions in the DSMC simulation. In addition to this, a velocity distribution also needs to be specified. The simplest method is to assume a Maxwellian distribution of velocities at the inflow. This is not strictly correct and the accuracy of this assumption and its effect on the simulations are assessed in the next section.

8.2.1 Flow field Results

Initially simulations were performed with the flow assumed to expand into vacuum. Figure 8.2 shows the number density contours obtained from these simulations. It can be seen that in the back flow region the number density is of the order of $1 \times 10^{18} m^{-3}$. In Bailey's report the back pressure is reported to be about and 2×10^{-5} torr. At temperatures of 300K this corresponds to a number density of $6.77 \times 10^{17} m^{-3}$. This suggests that the back pressure could influence the flow field in this region. Thus from this simulation it can be observed that the back pressure needs to be simulated to obtain a closer simulation of the experimental set-up. Figure 8.3 shows the number density contours obtained from simulations with a

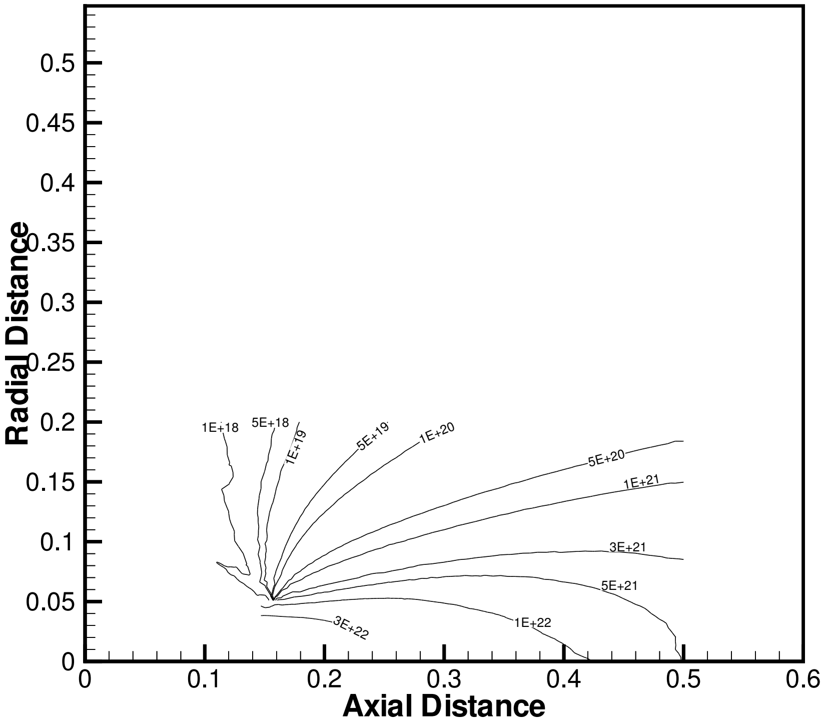

Figure 8.2. Number density profiles for simulations of CO2 expanding into vacuum back pressure of 2×10^{-5} torr.

8.2.2 Comparison with experiments

Two experimental measurements are performed in the back flow region. Carbon di-oxide number density measurements were accomplished using the electron beam fluorescence technique. Radial profiles of number density were measured and a smoothed spatial map of constant number density was derived. Figure 8.4 shows the comparison of the number density measurements with the number density obtained from the simulations. The agreement between the simulation results and the measured values deteriorate as we go into the back-flow region. The simulations

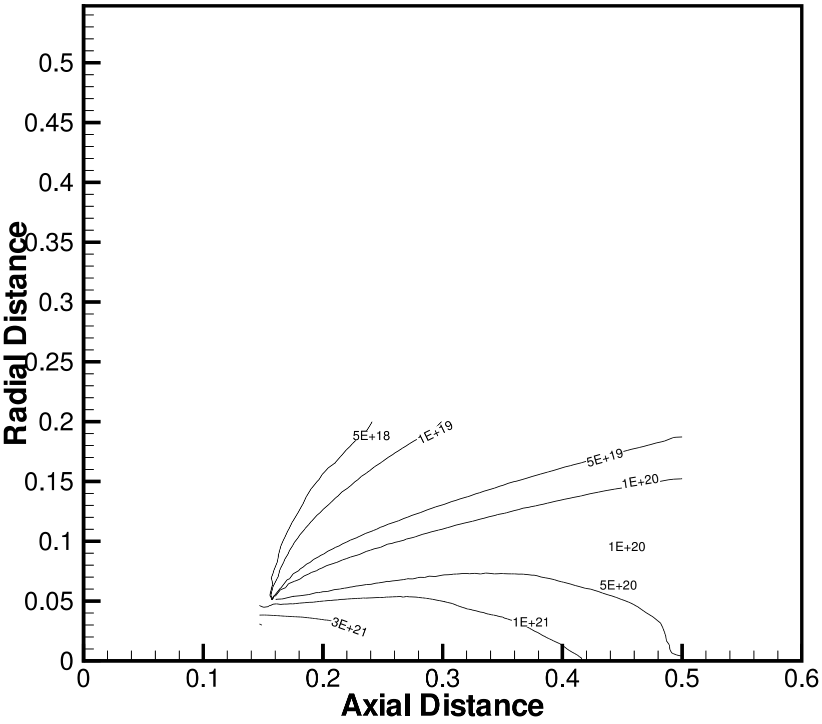

Figure 8.3. Number density profiles for simulations with ambient number density of 6.77e17 / m^3

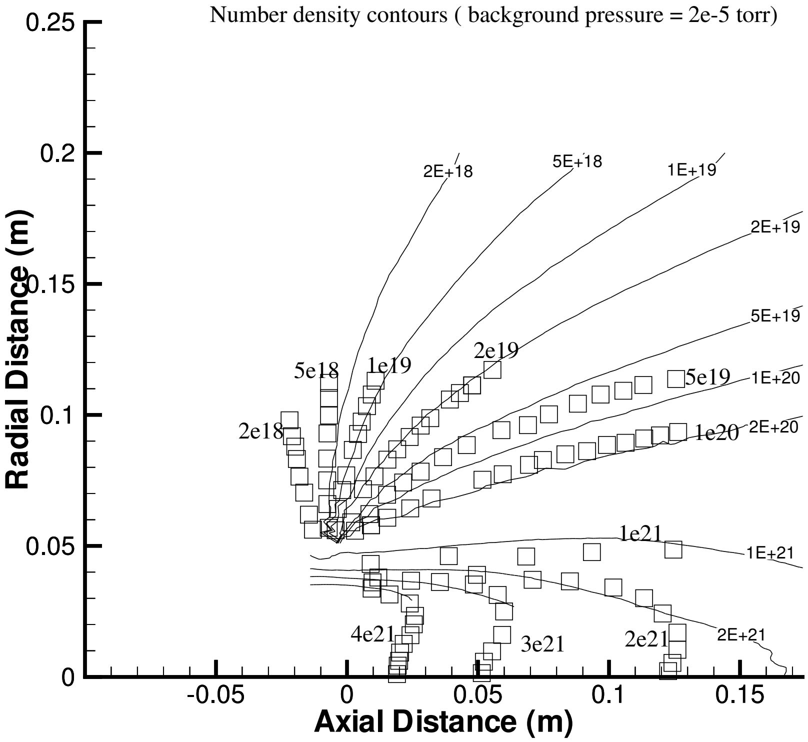

Figure 8.4. Comparison of measured and calculated data for the number density in the back-flow region

have an ambient number density of $6.77 \times 10^{17} m^{-3}$, which corresponds to a pressure of 2×10^{-5} torr and a temperature of 300K. It is possible that the actual ambient number density is higher than $6.77 \times 10^{17} m^{-3}$ and that would explain why the computed results are lower than the experimental measurements.

Figure 8.5 shows the number density contours obtained from a simulation with ambient number density set at $1 \times 10^{18} m^{-3}$. particles / m^3. Figure 8.6 shows a comparison of number density contours obtained from simulations with an ambient number density of 1e18. This sensitivity study shows that the ambient number density has a strong influence on in the regions where experimental measurements are made. Since the exact modeling of the back pressure distribution in the chamber

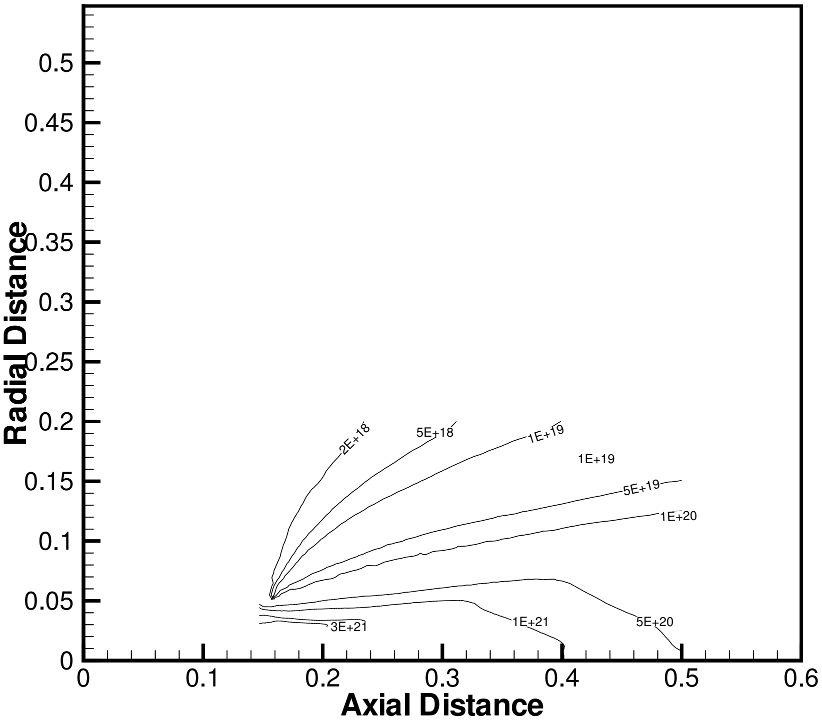

Figure 8.5. Number density profiles for simulations with an ambient number density of $1 \times 10^{18} m^{-3}$

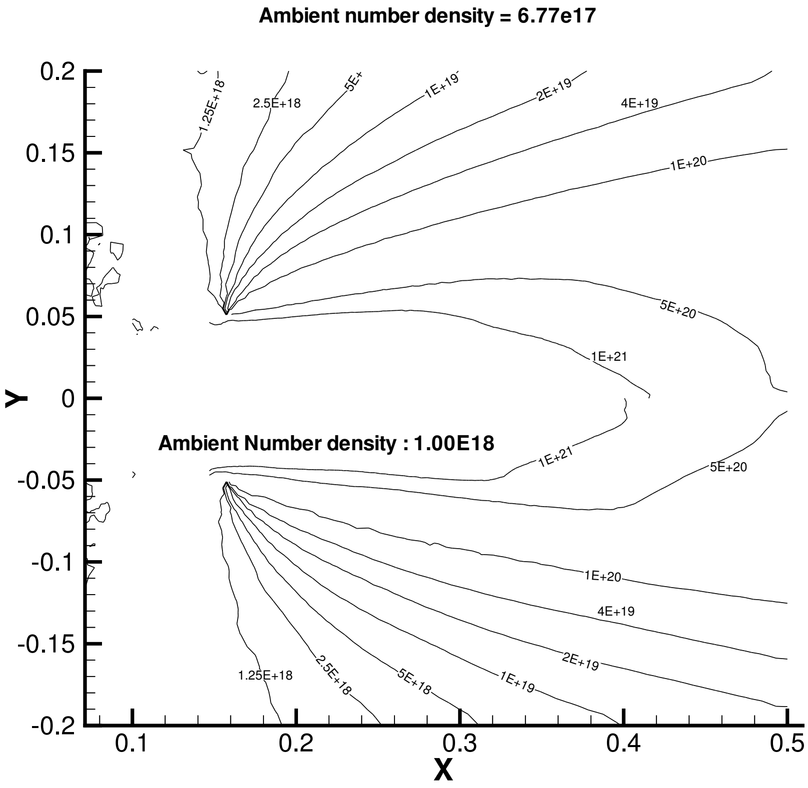

Figure 8.6. Comparison of number density profiles for simulations with an ambient number density of $1 \times 10^{18} m^{-3}$ and and ambient number density of $6.77 \times 10^{17} m^{-3}$

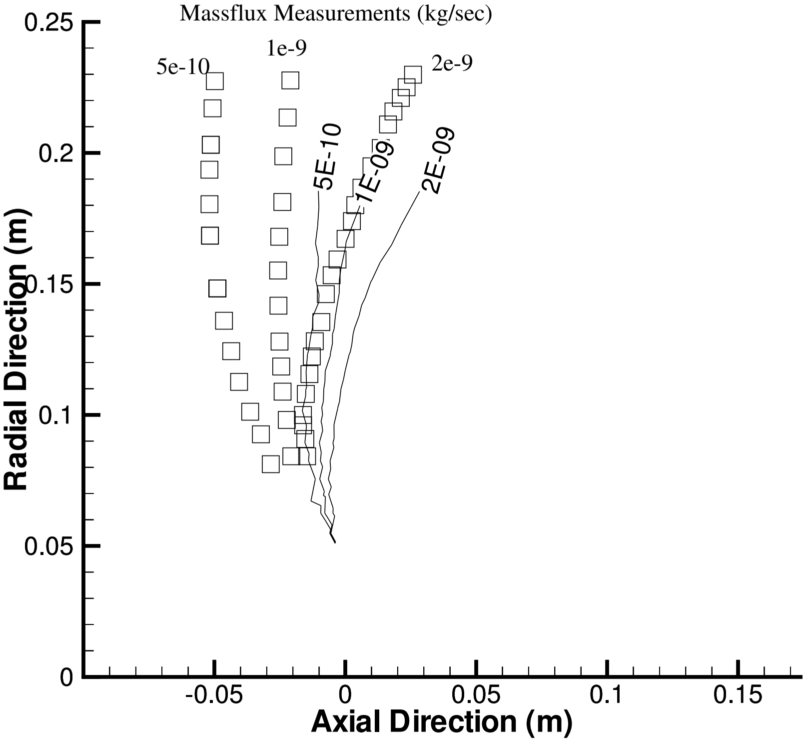

Figure 8.7. Comparison of measured and calculated data for the mass flow rate in the back-flow region

is very difficult, this suggests that further improvement in the agreement between computed and measured values is difficult.

Mass flux measurements were made in the back-flow region using a Quartz crystal microbalance. Figure 8.7 shows a comparison of the mass-flux measurements and the values calculated from the experiments. Summaries of the experimental measurements were presented as constant mass flux contours and compared with numerical results. Since there are only three contours it is difficult to make details comparisons but the results are consistent with the number density results.

8.3 DSMC computation with Chapman-Enskog boundary condition

This section presents the results of the investigation of a more accurate method of passing information from the CFD simulations to the DSMC simulation. The results from this new method are compared with the old method and experimental measurements.

8.3.1 Rationale

The boundary conditions for the DSMC simulations are set using the results from the CFD simulation. The gas properties (number density, temperature and velocity) need to be specified at the domain inlet. A velocity distribution function also needs to be specified at the inlet. Normally in DSMC simulations, thermodynamic equilibrium is assumed at the boundary and the velocity distribution is set using the Maxwell-Boltzmann distribution,

$$f_0(C) = \frac{1}{\pi^{3/2}} exp(-C^2), \tag{8.1}$$

where C = c / $(2kT/m)^{1/2}$ is the normalized thermal velocity, c is the velocity, k is the Boltzmann constant, T is the temperature and m is the particle mass. The results in the preceding section were obtained using this method.

For non-equilibrium flows, the Chapman-Enskog distribution is a better approximation. The Chapman-Enskog perturbation expansion of the Boltzmann equation gives, to first order in Sonine polynomial expansion, the distribution

$$f(C) = f_0(C)\Gamma(C), \tag{8.2}$$

where

$$\Gamma(C) = 1 + (q_xC_x + q_yC_y + q_zC_z)(\tfrac{2}{5}C^2 - 1)$$
$$-2(\tau_{x,y}C_xC_y + \tau_{x,z}C_xC_z + \tau_{y,x}C_yC_z)$$
$$-\tau_{x,x}(C_x^2 - C_z^2) - \tau_{y,y}(C_y^2 - C_z^2) \tag{8.3}$$

and

$$q_i = -\frac{\kappa}{P}(\frac{2m}{kt})^{1/2}\frac{\partial T}{\partial x_i} \tag{8.4}$$

$$\tau_{i,j} = -\frac{\mu}{P}(\frac{\partial v_i}{\partial x_j} + \frac{\partial v_j}{\partial x_i} - \frac{2}{3}\frac{\partial v_k}{\partial x_k}\partial_{i,j}) \tag{8.5}$$

where $\tau_{i,j}$ and q_i are the dimensionless heat flux and the stress tensor[16]. The viscous and thermal conductivity are μ and κ, respectively.

8.3.2 Implementation

The Chapman-Enskog distribution is implemented using an acceptance rejection technique described in Garcia[16]. An envelope function $g(C)$ is defined such that $g(C) > f(C)$ for all C. Then a random point from the region beneath g(C) is selected. All points in this region are equally likely to be selected. A simple way to select this point is to use g(C) = A $f_0(C)$, where $f_0(C)$ is the Maxwell-Boltzmann distribution. A velocity C_{try} is drawn from $f_0(C)$ and is accepted if this point lies beneath f(C). Otherwise a new point is drawn and the procedure is repeated. More details about this procedure are described by Garcia[16].

At the interface between the two domains $\Gamma(C)$ has a value of about 0.95. Figure 8.8 shows the contours of the Chapman-Enskog parameter calculated using

[c] 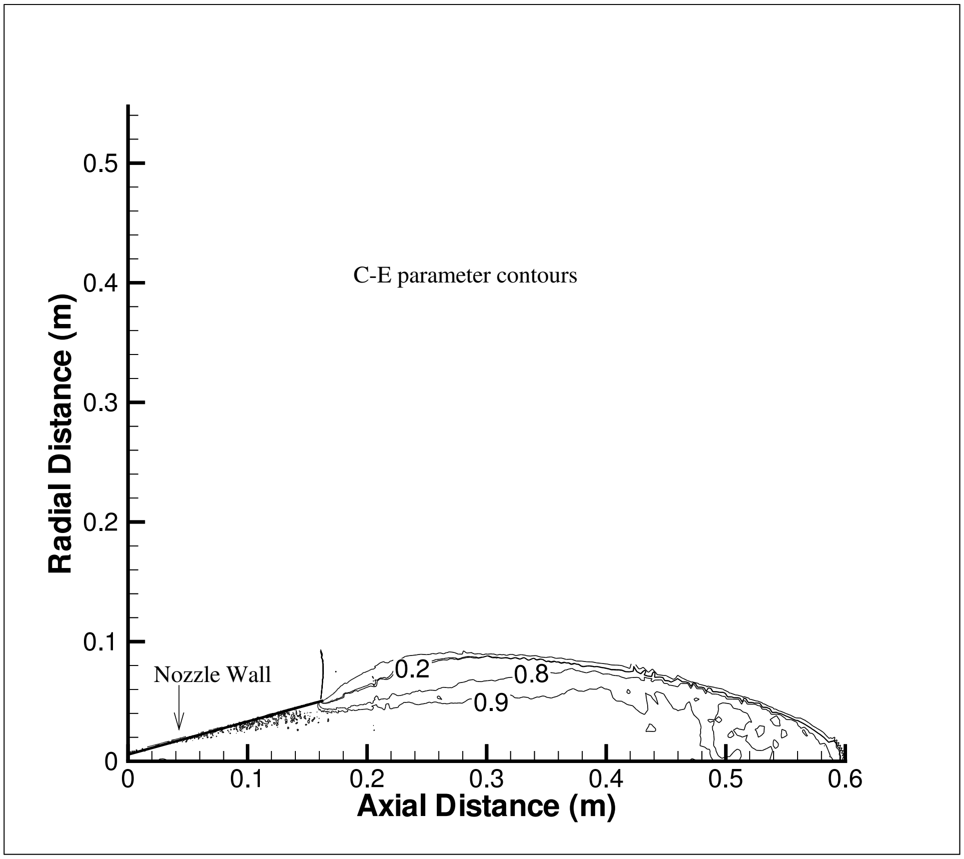

Figure 8.8. Contours of Chapman-Enskog parameter calculated based on the CFD solution

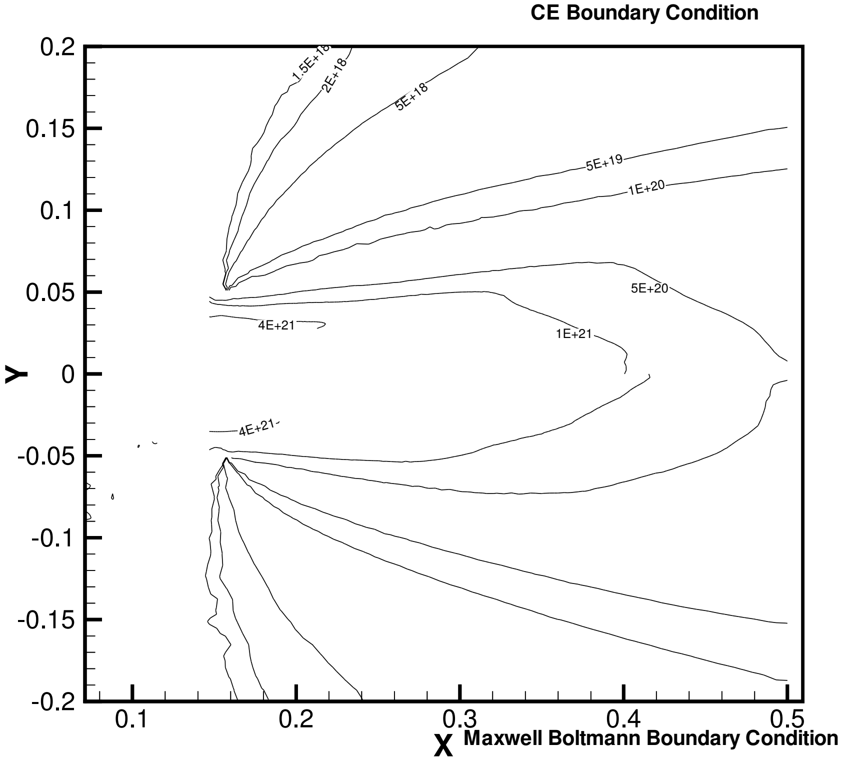

Figure 8.9. Comparison of contours of number density

the mean velocity. As described in the previous chapter, a value of $\Gamma(C) = 0.95$ is assumed to be a safe indication of the validity of Navier-Stokes equations.

8.3.3 Comparison of results

The objective of this section is to compare the two different methods of passing information. Figure 8.9 shows a comparison of the number density contours obtained from the two methods. The agreement between the two methods is fairly good and there does not seem to be any appreciable difference between the two results.

Figure 8.10 shows a more detailed comparison of the number density at a radial

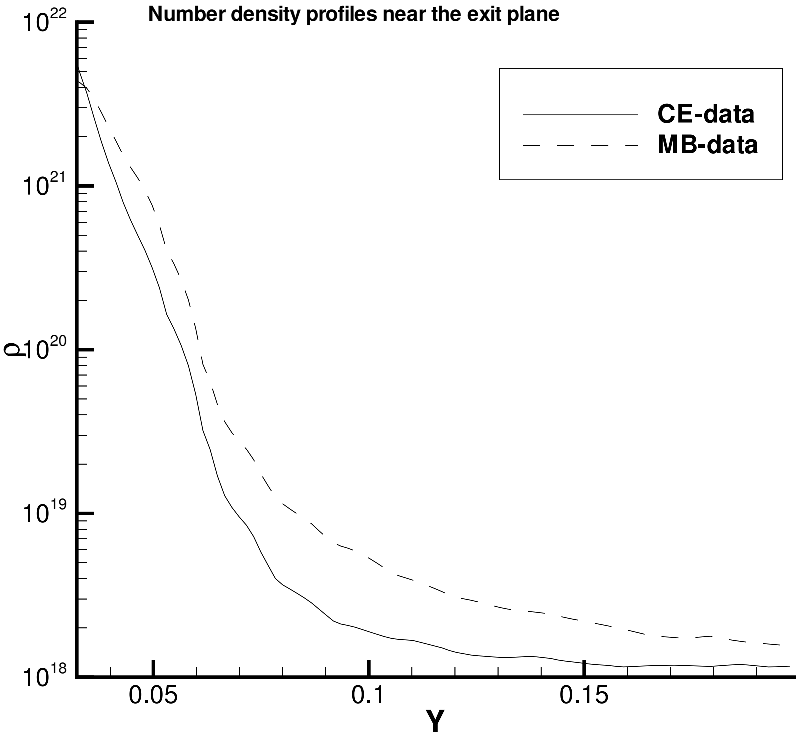

Figure 8.10. Number density along a radial section at the exit plane

section along the exit plane of the nozzle. This comparison shows few differences although the over all behavior is very similar. The results obtained from the application of the Chapman-Enskog boundary condition are lower than the results from the Maxwell-Boltzmann boundary conditions.

Figure 8.11 and figure 8.12 shows a comparison of these results with the experimental measurements. The comparisons are very similar to the comparisons obtained from the Maxwell-Boltzmann results. It is difficult to assess the importance of using the Chapman-Enskog boundary conditions from these results. More detailed measurements in the back-flow region is required to perform a more detailed analysis of the two boundary conditions. In this study the results obtained

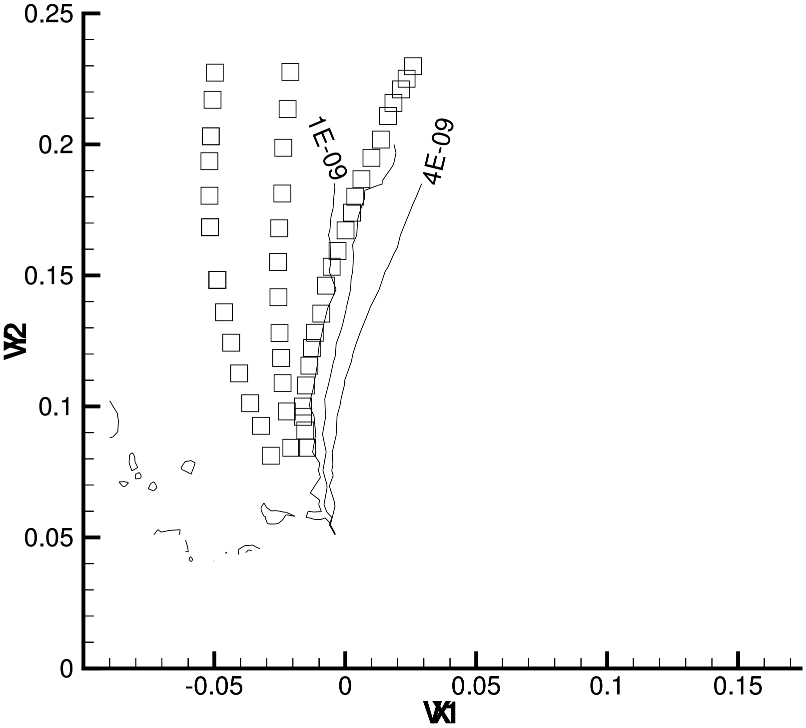

Figure 8.11. Comparison of measured and calculated data for the number density in the back-flow region

from the two boundary conditions are similar.

8.4 Conclusions

The objective of this study was to investigate different methods of performing back flow simulations. The combined CFD-DSMC method can be used to obtain results in the back flow region. The back flow region was found to be very sensitive to the ambient conditions and an accurate simulation of the back pressure is essential. The simulation results show lower number densities than observed experimentally. A more accurate assessment of these issues requires more measurements to compare

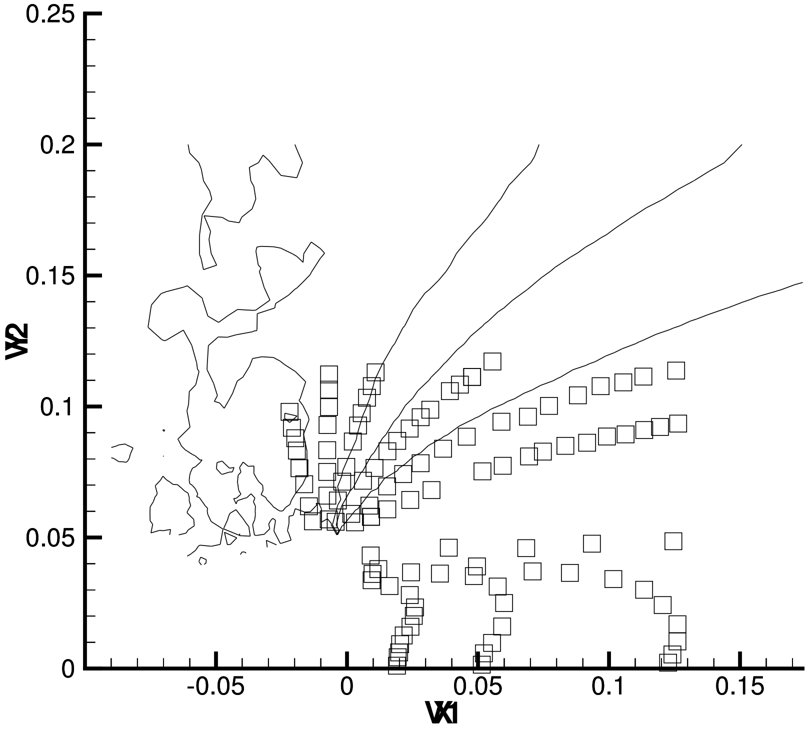

Figure 8.12. Comparison of measured and calculated data for the mass flow rate in the back-flow region

the numerical results. Two methods for transferring information to the DSMC simulation are compared. The two methods were found to give very similar results and so Maxwell Boltzmann boundary conditions were found to be sufficient.

Chapter 9

Summary and conclusions

The objective of this dissertation was to develop a methodology for performing simulations of a complete nozzle plume system. A combined CFD-DSMC approach for performing these simulations was developed.

The combined approach involves four steps. First, a continuum simulation of the nozzle plume system is performed. An unstructured Navier-Stokes solver for performing these simulations was developed. The next step involves predicting the breakdown of Navier-Stokes equations from the CFD simulations and dividing the domain into a CFD region and a DSMC region. Various parameters that could be used for this were investigated and a new parameter was proposed. The third step involves transferring information from the CFD simulation to the DSMC simulation. Different methods of transferring information were analyzed. The last step involves performing DSMC simulations. DSMC simulations were performed and the results were analyzed to understand more about the breakdown of the Navier-Stokes equations.

The method was applied to the study of two nozzle systems for which experimental results were available. The first system involved was a hydrogen thruster. A kinetics model for hydrogen consistent with a previously developed DSMC model was implemented. It was successfully applied to investigate the low-density hydrogen plume flows.

The comparison between the numerical results and experimental measurements was found to be good in terms of overall flow features. For a more detailed quantitative comparison higher resolution experimental measurements are required. The experimental measurements could not be used to differentiate between the two computational methods. An assessment of the validity of some of the equilibrium relations used for data reduction also needs to be performed. An important conclusion of this study is that these solutions exhibit a high degree of grid dependence. This was found to be true of both the DSMC and CFD computations. Thus care should be taken to ensure that the grid resolution is fine enough to obtain accurate results. This emphasizes the importance of flexible gridding techniques provided by the use of unstructured grids. For this system, it is difficult to separate the results of the grid dependence from the physics of the problem. An exhaustive grid independence study was not carried out since it would not add to our understanding of the flow. Further refinement of the grid did not improve the agreement with the experimental measurements.

The next system analyzed was the expansion of carbon di-oxide into vacuum. The computational results were found to be sensitive to the wall boundary condition. Experimental measurements of pitot pressure measurements along the centerline were compared with calculations based on the CFD simulations. The computed values were close enough to experimental measurements to suggest that the physics of the flow was captured accurately. Detailed relaxation modeling of the different energy modes of CO_2 indicated that the vibrational mode was frozen in the diverging portion of the nozzle and in the plume. The CFD simulations also predicted regions of rotational non-equilibrium inside the plume. The central core region of the flow was non-isentropic and had a ratio of specific heats, γ close to 1.2. This invalidates the isentropic flow assumption and the value of γ of 1.4 used for calibrating some of the experimental measurements. The computations re-confirmed earlier findings about the behavior of the flow near the nozzle lip. Flow angle measurements were compared with the computed values and found to agree in the central-core region of the flow. The CFD predictions of radial profiles of number density showed good agreement within regions of validity of the continuum approach.

A breakdown parameter was used to split the domain by predicting the breakdown of the Navier-Stokes equations. DSMC simulations were performed of regions where CFD methods are not accurate, were performed. The DSMC predictions of radial number density profiles were then compared with the experimental measurements and found to be in good agreement, even in regions where the CFD results disagree with experiments. DSMC results were analyzed in detail in an attempt to investigate the failure of the CFD approach. It was found that the regions where CFD results are inaccurate corresponded with regions of translational non-equilibrium. Since the Navier-Stokes equations are based on the assumption of translational equilibrium, solutions to Navier-Stokes equations give inaccurate results for such flow regimes.

9.1 Future Research

There are three broad areas where further research should be conducted. The first area is improving the methodology. The transfer of information from the CFD simulation to the DSMC simulation could be investigated in more detail. In these simulations the gradient information is lost when the data from the CFD simulation is transferred to the DSMC simulations. The set of experimental data should be used to investigate differences between different methods of data transfer. The back-flow simulations should be analyzed in more detail to investigate these issues. The experimental sets investigated in this thesis did not have sufficient data in the back flow regime to make meaningful comparisons.

The second area of further research is in developing the models for physical phenomena. The focus of this investigation was on developing the methodology. Another investigation should be carried out to investigate the validity of the models used and develop better modeling techniques.

The third area of further research is in the numerical technique. The use of unstructured grids offers the possibility of the use of adaptive solution methodologies. These techniques should be investigated to improve the efficiency of the continuum code.

Bibliography

[1] I. D. Boyd, P. F. Penko, D. L. Meissener and K. J. Dewitt, *“Experimental and Numerical Investigations of Low-density Nozzle and Plume Flows of Nitrogen,”* AIAA Journal, Vol 10 (10), 1992, pp. 2453-2461

[2] P. F. Penko, I. D. Boyd, D. L. Meissener and K. J. Dewitt, *“Analysis and Measurement of a Small Nozzle Plume in Vacuum,”* Journal of Propulsion and Power, Vol. 9, 1993, pp. 646-648.

[3] I. D. Boyd, M. A. Capelli and D. R. Beattie, *“Monte Carlo Computation of Nozzle and Plume Flows of a Low-Power Hydrogen Arcjet,”* AIAA Paper 93-2529, Monterey, Ca, June 1993

[4] I. D. Boyd, D. R. Beattie and M. A. Capelli, *“Monte Carlo and Experimental Studies of Chamber Effects for a Low-Power Hydrogen Arcjet,”* International Electric Propulsion Conference, September 1993

[5] Boyd I. D., Jafry Y., and Vanden Beukel, J., *”Particle Simulation of Helium Microthruster Flows,”* Journal of Spacecraft and Rockets, Vol. 31, 1994, pp. 271-277.

[6] Blottner, F. G, Johnson, M. and Ellis, M. *”Chemically Reacting Viscous Flow Program for Multi-Component Gas Mixtures,”* Report No. SC-RR-70-754, Sandia Laboratories, Albuquerque, New Mexico.

[7] C. R. Wilke, *“A Viscosity Equation for Gas Mixtures,”* Journal of Chem. Phys., 18, pp. 517-519

[8] , *The computation of Weakly Ionized Hypersonic Flows in Thermo-Chemical Nonequilibrium* Stanford University, June 1998

[9] A. B. Bailey and L. L. Price, *“Flow Field Mapping of Carbon Dioxide Nozzle Expansion into Vacuum,”* AEDC-TR-85-26.

[10] J. D. George and I. D. Boyd, *“The numerical investigation of hydrogen plume flows using unstructured grids,”* AIAA Paper 98-2448, June. 1998.

[11] M. Camac,*"CO_2 Relaxation Processes in Shock Waves,"* in *"Fundamental Phenomena in Hypersonic Flow edited by J. G. Hall,"* Cornell University Press, 1966, p. 195.

[12] I. D. Boyd, P. F. Penko and L. M. Carney,*"Efficient Monte Carlo Simulation of Rarefied Flow in a Small Nozzle,"* AIAA 90-1693

[13] G. A. Bird, *"Breakdown of Continuum Flow in Freejets and Rocket Plumes,"* Proceedings of

the Twelfth International Symposium on Rarefied Gas Dynamics, Vol. 74, Part II, Progress in Astronautics and Aeronautics, AIAA, New York, 1981, pp. 681-694.

[14] I. D. Boyd , Gang Chen and G. V. Candler, *"Predicting failure of the continuum fluid equations in transitional hypersonic flows,"* Physics of fluids, Vol 7, No. 1, 1995, pp. 210-219 .

[15] G. A. Bird, *" Breakdown of translational and rotational equilibrium in gaseous expansions"* , AIAA Journal , Vol 8, 1970, pp. 1990.

[16] A. L. Garcia and B. J. Alder, *"Generation of the Chapman-Enskog distribution,"* Journal of Computational Physics, 140, 1998, pp. 66-70.

[17] S. Dietrich and I. D. Boyd, *"Scalar and Parallel Optimized Implementation of the Direct Simulation Monte Carlo Method,"* Journal of Computational Physics, Vol. 126, 1996, pp. 328-342.

[18] G. A. Bird, *"Direct Simulation of High Vorticity Gas Flows,"* Physics of Fluids, Vol. 30, 1987, pp. 364-366.

[19] I. D. Boyd, D. R. Beattie and M. A. Capelli, *"Numerical and Experimental Investigations of Low-Density Supersonic Jets of Hydrogen,"* Journal of Fluid Mechanics, Vol. 280, 1994, pp. 41-67.

[20] J. G. Parker, *"Comparison of Experimental and Theoretical Vibrational Relaxation Times for Diatomic Gases,"* Journal of Chemical Physics, Vol. 41, pp. 1600-1609.

[21] R. W. MacCormack and G. V. Candler, *"The Solution of Navier-Stokes Equations Using Gauss-Siedel Line Relaxation,"* Computers and Fluids, Vol. 17, No.1, 1989, pp. 135-150.

[22] J. T. Batina, *"Unsteady Euler Airfoil Solutions Using Unstructured Dynamic Meshes,"* AIAA Journal, Vol. 28, No. 8, 1990, pp. 1381-1388.

[23] T. J. Barth and D. C. Jespersen, *"The Design and Application of Upwind Schemes on Unstructured Meshes,"* AIAA Paper 89-0366, Jan. 1989.

[24] D. Pan and J. C. Cheng, *"Upwind Finite-Volume Navier-Stokes Computations on Unstructured Triangular Meshes,"* AIAA Journal, Vol. 31, No. 9, 1993, pp. 1618-1625.

[25] I. D. Boyd, P. F. Penko,D. L. Meissner and K. J. Dewitt, *"Experimental and Numerical Investigations of Low-Density Nozzle and Plume Flows of Nitrogen,"* AIAA Journal, Vol. 30, 1992, pp. 2453-2461.

[26] P. F. Penko, I. D. Boyd, D. L. Meissner and K. J. Dewitt, *"Measurement and Analysis of a Small Nozzle Plume in Vacuum,"* Journal of Propulsion and Power, Vol. 9, 1993, pp. 646-648.

[27] J. D. George and I. D. Boyd, *"The numerical investigation of hydrogen plume flows using unstructured grids,"* AIAA Paper 98-2448, June. 1998.

[28] K. C. Kannenberg and I. D. Boyd, *"Three dimensional Monte Carlo simulations of plume impingement,"* Journal of Thermophysics and Heat Transfer, Vol. 13, 1999, pp. 226-235.

[29] G. Chen and I. D. Boyd, *"Statistical error analysis for the direct simulation Monte Carlo method,"* Journal of Computational Physics, Vol. 126, 1996, pp. 434-448.

[30] I. D. Boyd, *"Analysis of rotational nonequilibrium in standing shock waves of nitrogen,"* AIAA Journal, Vol. 28 (11), 1990, pp. 1997-1999.

[31] I. D. Boyd, *"Analysis of vibrational-translational energy transfer using the direct simulation Monte Carlo method,"* Physics of Fluids A, Vol. 3 (7), 1991, pp. 1785-1791.

[32] T. Abe, *Direct simulation Monte Carlo method for internal-translational energy exchange in nonequilibrium flow,"* Rarefied Gas Dynamics, Vol. 159, AIAA, 1992, pp. 103-113.

[33] D. Baganoff and J.D. McDonald, *A collision selection rule for a particle simnulation method suited to vector computers,"* Physics of Fluids A, Vol. 2, 1990, pp. 1248-1259.

[34] R.W. MacCormack and G. V. Candler, *"The solution of the Navier-Stokes equations using Gauss-Seidel line relaxation,"* Computers and Fluids, Vol 17 (1), 1989, pp. 135-150.